2014-03-18

Spin and Orbital Moments and Magnetic Order in Fe3O4 Nanoparticle Assemblies

Yanping Cai
Brigham Young University - Provo

Spin and Orbital Moments and Magnetic Order in Fe$_3$O$_4$ Nanoparticle Assemblies

Yanping Cai

A thesis submitted to the faculty of
Brigham Young University
in partial fulfillment of the requirements for the degree of

Master of Science

Karine Chesnel, Chair
Branton Campbell
Roger Harrison

Department of Physics and Astronomy

Brigham Young University

March 2014

ABSTRACT

Spin and Orbital Moments and Magnetic Order in Fe_3O_4 Nanoparticle Assemblies

Yanping Cai
Department of Physics and Astronomy, BYU
Master of Science

Fe_3O_4 magnetic nanoparticles of 5 to 11 nm in size were prepared by organic methods. Particle size was analyzed by both X-ray Diffraction (XRD) and Transmission Electron Microscopy (TEM) techniques. Zero Field Cooling (ZFC) / Field Cooling (FC) and magnetization loop measurements were recorded by VSM, and they confirmed superparamagnetic behavior in the sample. The blocking temperature is found to be in the range of 30 K $\sim$ 170 K. It has a dependence on the particle size. ZFC / FC curves also indicate the presence of magnetic coupling between particles. X-ray Magnetic Circular Dichroism (XMCD) measurements of these nanoparticles were measured at 80 K and 300 K. By using the sum rules, spin and orbital magnetic moments were calculated from the XMCD signal. The results confirm a quenching orbital moment and a large spin moment. The calculated total magnetic moments are somewhat smaller than in bulk Fe_3O_4. Also, the spin moment at 80 K was found to be larger than at 300 K. X-ray Resonant Magnetic Scattering (XRMS) measurements at different temperatures, polarizations and fields were carried out. The intensity profile gives information on the interparticle distance between nanoparticles which is consistent with TEM results. A magnetic signal was extracted by calculating the dichoroic term, when the energy is tuned to resonant edges. This magnetic signal is confirmed by comparing the dichroic terms at different conditions.

ACKNOWLEDGMENTS

Contents

Chapter 1

Introduction

1.1 Background

The study of nanomaterials and nanotechnologies has been booming in the last several decades. Among thousands of different kinds of nanomaterials, magnetic nanoparticles have attracted special attentions because of their important role in biomedicine and nanotechnology. [1] Magnetic nanoparticles have been proven to be an excellent material when it comes to applications. These include drug targeting, bioseparation, cancer therapy such as hyperthermia and magnetic resonance imaging (MRI) techniques. [2–4] Magnetite (Fe_3O_4) has advantages such as non-toxicity to the human body, long circulation in the blood stream, and the ability to be highly functionalized, when it is used in these medical applications. [5] The structural and magnetic properties of bulk Fe_3O_4 have been broadly studied and are well established. Fe_3O_4 has a high Curie temperature at around 850 K. Below this temperature, it exhibits ferrimagnetic order, with three different types of spins carried by Fe^{2+} and Fe^{3+} ions. Fe_3O_4 also has a renowned metal-insulator transition at 120 K, which is usually called the Verwey transition. [6] However, these bulk properties can be altered when the size of Fe_3O_4 comes down to nanoscale. One essential magnetic property arising from

Fe_3O_4 nanoparticle assemblies is their superparamagnetic behavior, where each particle, suppos-edly monocrystalline, behaves as a single ferromagnetic domain. These nanoparticles, carrying a giant magnetic moment, then magnetically interact and fluctuate in the nanoparticle assembly. [7] In order to understand the structure and magnetic behavior of magnetite nanoparticles better, we fabricated a set of magnetite nanoparticles with different sizes and studied them via X-ray Diffrac-tion (XRD), Transmission Electron Miscroscopy (TEM), Vibrating Sample Magnetometer (VSM), as well as synchrotron experiments such as X-ray Magnetic Circular Dichroism (XMCD) and X-ray Magnetic Resonant Scattering (XRMS). In Chapter 2, I will present the fabrication methods along with the characterization results. Then I will discuss the method to calculate the spin and orbital moments of Fe_3O_4 with X-ray Magnetic Circular Dichroism (XMCD) spectra in Chapter 3. Lastly, I will discuss the way to obtain magnetic signals through X-ray Resonant Magnetic Scattering (XRMS) experiments.

Chapter 2

Nanoparticle Preparation and Characterization

2.1 Nanoparticle fabrication

Various ways have been used to fabricate Fe_3O_4 nanoparticles, including both inorganic and organic methods. We synthesized four different sizes of Fe_3O_4 nanoparticles using three different organic solution methods. All of them involve the thermal decomposition of an iron precursor. [8–12] To control the particle size, we adjusted the reaction temperature and reaction solution, as it has been observed that these parameters impact the size of particles. [13] The smallest nanoparticles of average size 5 nm (NP15, Method 1), were fabricated by heating an iron(III) oleate in oleic acid and octadencene. [14] The iron (III) oleate was prepared by slowly adding a methanol solution of NaOH to a methanol solution of $FeCl_3 \bullet 6H_2O$ and oleic acid, filtering the mixture and letting them dry under vacuum overnight. [15] To form the nanoparticles, the iron (III) oleate was added to oleic acid and octadecene, heated to 300 °C for 30 min, and cooled to room temperature. The nanoparticles were then precipitated with ethanol and isolated by centrifugation and decanting.

Table 2.1 A summary of all the synthetic methods and flux temperatures.

Sample Name	Method	Reflux Temperature
NP15	Method 1	322 °C
NP16	Method 1	320 °C
NP17	Method 2	290 °C
NP18	Method 3	260 °C

The largest nanoparticles of average size 11 nm (NP16, Method 1), were prepared following a similar procedure to NP15, but at higher temperature and with more octadecene. The iron (III) oleate was also mixed with oleic acid and octadecene but heated at 320 °C for 30 min rather than 300 °C.

The intermediate size nanoparticles of average size 8 nm (NP17, Method 2), were fabricated from iron acetylacetonate. [16] In this preparation, Fe (III) acetylacetonate was mixed with hexadecane, octadecene, oleic acid and oleyamine. The mixture was heated to 200 °C for another 30 minutes, and cooled to room temperature. The resulting nanoparticles were precipitated with ethanol and isolated. We also prepared NP18 which was used in the XMCD experiments. NP18 has a size of 5.6 nm. It followed the same preparation methods as NP17 except we used phenylether instead of octadecene (Method 3). All the samples were subsequently deposited onto Si_3N_4 membranes, where the nanoparticles self-assembled and formed a hexagonal lattice. The concentration of the solution was optimized to reach a close packed monolayer of nanoparticles. Table 2.1 shows a sumary of all the methods and different reflux temperatures.

2.2   Structural properties

X-ray Diffraction (XRD) measurements were used to study the crystallographic structure of our nanoparticles. In addition, we also used Transmission Electron Microscopy (TEM) to visualize the sample and estimate the average size.

A Tecnai F30 Transmission Electron Microscope (TEM) was used to take images of the nanoparticle assemblies. As seen in Figure 2.1, the shape of the nanoparticles is rather spherical. All the TEM images of the sample were taken at concentrations lower than the optimized one, because it is easier to obtain a statistical analysis of the sparsely deposited nanoparticles. We used the software package ImageJ to circle each nanoparticle visible in the image and evaluate their areas. Then, the area was converted to diameter in nm, and resulted in a histogram of size distributions. The analysis yields an average particle diameter of 5.3 ± 0.7 nm for sample NP15, 8.1 ± 1.7 nm for sample NP17 and 11.3 ± 2.5 nm for sample NP16. Sample NP15 has the smallest average size and narrowest size distribution, while sample NP17 and NP16 have relatively larger sizes and wider size distributions.

We used the PANalytical X'Pert instrument to perform X-ray Diffraction (XRD) measurements. As shown in Figure 2.1, all the samples exhibit a cubic $Fd3m$ structure, consistent with the inverse spinel structure of Fe_3O_4 magnetite. Magnetite (Fe_3O_4) and maghemite γ-Fe_2O_3 are very hard to distinguish via XRD scan alone because they have the same inverse spinel structure with very close lattice parameters and the XRD scan has very broad peaks and a noisy background. The rhombohedral hematite phase (α-Fe_2O_3) has a different structure, and can therefore be distinguished. However, our XRD scans for the three samples show no visible signs of hematite, which indicates a high purity of Fe_3O_4. It appears that the majority of the material is crystalline, because there are essentially no broad peaks that cannot be attributed to nanoparticles. By analyzing the peak widths in the XRD scan with the Scherrer equation below (Equation 2.1), we are able to

Table 2.2 A summary of all the organic methods and flux temperatures.

Sample Name	TEM(nm)	XRD(nm)
NP15	5.3 ± 0.7	5.8 ± 1.7
NP17	8.1 ± 1.7	8.5 ± 2.9
NP16	11.3 ± 2.5	11.0 ± 4.6

estimate the average crystallite grain size of these samples.

$$d = \frac{K\lambda}{B cos(\theta)} \tag{2.1}$$

In this equation, $K = 0.9$ according to our sample and the instrument calibration. λ is equal to the x-ray wavelength, which is 0.15418 nm. B is measured and is the width of the peak at half maximum. θ is the position of the peak. The average size was found to be 5.8 ± 1.7 nm for sample NP15, 8.5 ± 2.9 nm for sample NP17 and 11.0 ± 4.6 nm for sample NP16. The results are in reasonably good agreement with the TEM results, with crystalline grain size $\cong$ particle size in the TEM image, thus each particle is monocrystalline. The slight size discrepancies between the TEM and XRD results are mostly attributable to the large noise in the XRD scan, which is due to the small amount of material used for the XRD measurements. All the sizes measured by XRD and TEM techniques are listed in Table 2.2.

2.3 Magnetic behavior

The magnetic behavior of the magnetic nanoparticles was investigated at different temperatures, from 20 K to 400 K, under an external magnetic field, using a Vibrating Sample Magnetometer (VSM). VSM uses Faraday's law to measure magnetic properties of a given material. Fe_3O_4 has
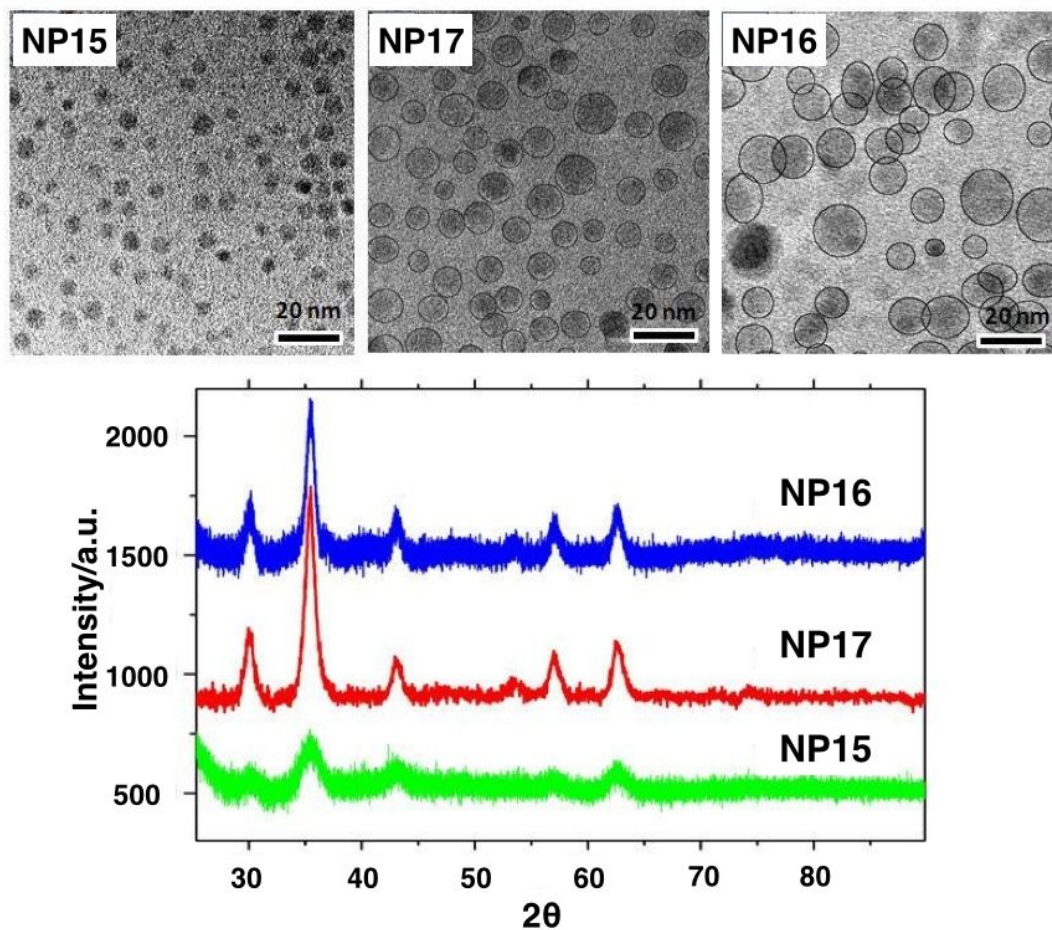
Figure 2.1 (Top) 100 nm TEM images of Fe$_3$O$_4$ nanoparticles NP15 5.3 nm NP17 8.1 nm NP16 11.3 nm; (bottom) XRD scans of the three samples NP15, NP17 and NP16

three different types of Fe ions with different magnetic moments. It results in a ferrimagnetic be-havior in the monocrystalline nanoparticle. The magnetic moment of the ions in the nanoparticle are aligned in the ferrimagnetic order, thus creating a giant magnetic moment carried by nanopar-ticle. These giant magnetic moments are randomly oriented at high temperature, which leads to a paramagnetic-like behavior at the nanoscale. [7] Figure 2.2(a) shows magnetization curves for the intermediate size, sample NP17, measured at 400 K, 300 K, 80 K and 20 K. The general shape of the curves is very sharp at $300 \sim 400$K. By comparing the Langevin model of paramagnetism in Figure 2.2(b), we find these curves to indicate paramagnetic behavior, here extended to superpara-magnetism in the nanoscale. The shape is visibly modified when the sample is cooled down.

The sharpness of the slope or susceptibility, at zero field ($H = 0$), is increased at lower tem-peratures. At lower temperature, the nanoparticles are magnetically blocked. In this blocked state, the magnetic coupling between nanoparticles is stronger. The total magnetic moment at the satu-ration field is also higher than at high temperature due to less thermal fluctuation, as we can see from Figure 2.2(b). [17] We find the hysteresis effects occur at low temperature, characteristic of a blocked state where the nanomagnets show a ferromagnetic-like behavior, leading to an opening of the magnetization loop around zero field, with a coercive field H_c of about 100 Oe at 20 K in the case of the 8 nm particles, as shown in Figure 2.3. We also measured the hysteresis effects for different samples at different temperature, as shown in Figure 2.4. Because the larger macro spin yields stronger magnetic coupling, the hysteresis effect increases as the sample size increases.

We also measured the magnetic response to cooling the sample down to 20 K. Figure 2.5(a) shows Zero Field Cooling (ZFC) together with Field Cooling (FC) curves for sample NP17. For the ZFC measurements, the particles were cooled to 20K with no field ($H = 0$) and then heated up to 400 K in the presence of a magnetic field of given magnitude H. For the FC measurements, the particles were cooled down and heated up in the presence of the magnetic field H. FC and ZFC curves were measured at different values H: from 50 Oe up to 500 Oe. Figure 2.5 (a) shows
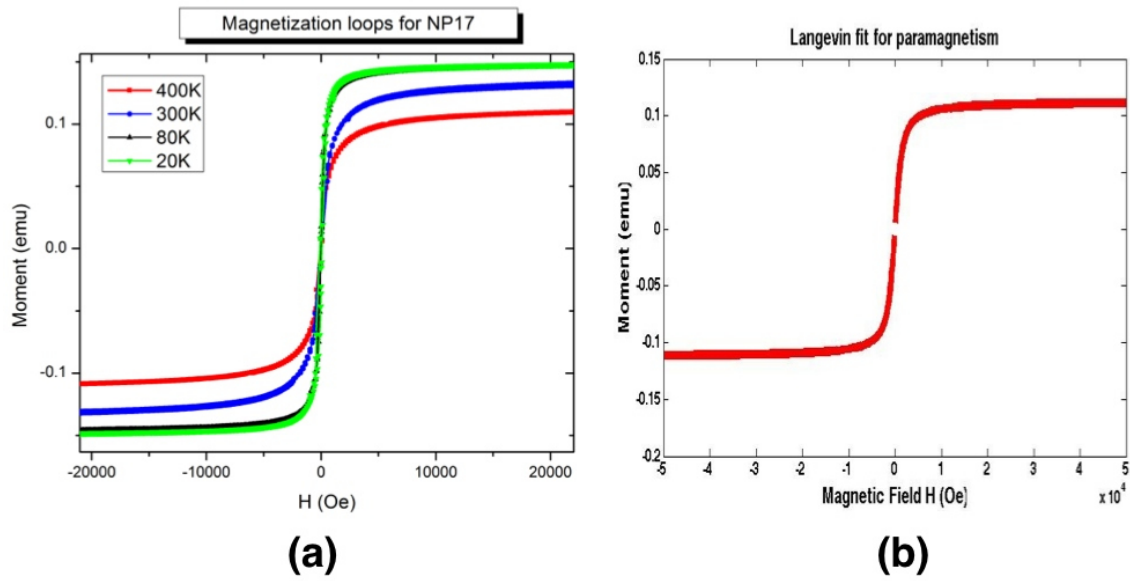
Figure 2.2 (a) Magnetization curves of sample NP17 (8nm) at 400, 300, 80 and 20K. (b) The simulation of Langevin model of paramagnetism, in our case, it extends to super paramagnetism.

the heating part of the FC and ZFC curves at selected field values. All the ZFC curves exhibit a peak, indicating a transition from a magnetically blocked state (at low temperature) to a superparamagnetic state (at high temperature). As expected, the position T_{max} of the peak varies with the magnitude H of the external field due to the competition between the inter-particle dipolar magnetic couplings, thermal activation and the magnetic interaction with the external field (Zeeman effect). T_{max} increases when the external field H decreases and approaches zero as shown in Figure 2.5(b). It appears that for sample NP17, T_{max} reaches an optimal value of 130 K when H is 75 Oe or smaller. We ascribe this temperature to the blocking temperature, here $T_B = 130$ K, for these intermediate size Fe_3O_4 nanoparticles. ZFC and FC curves will join when the macro spins of nanoparticles in both the ZFC and FC cases align with the field in the same way. T_{max} means the time when the magnetic moment is at the maximum. T_{max} occurs first, and when there is more thermal energy added to the system, the magnetic coupling is fully overcome, which leads to the
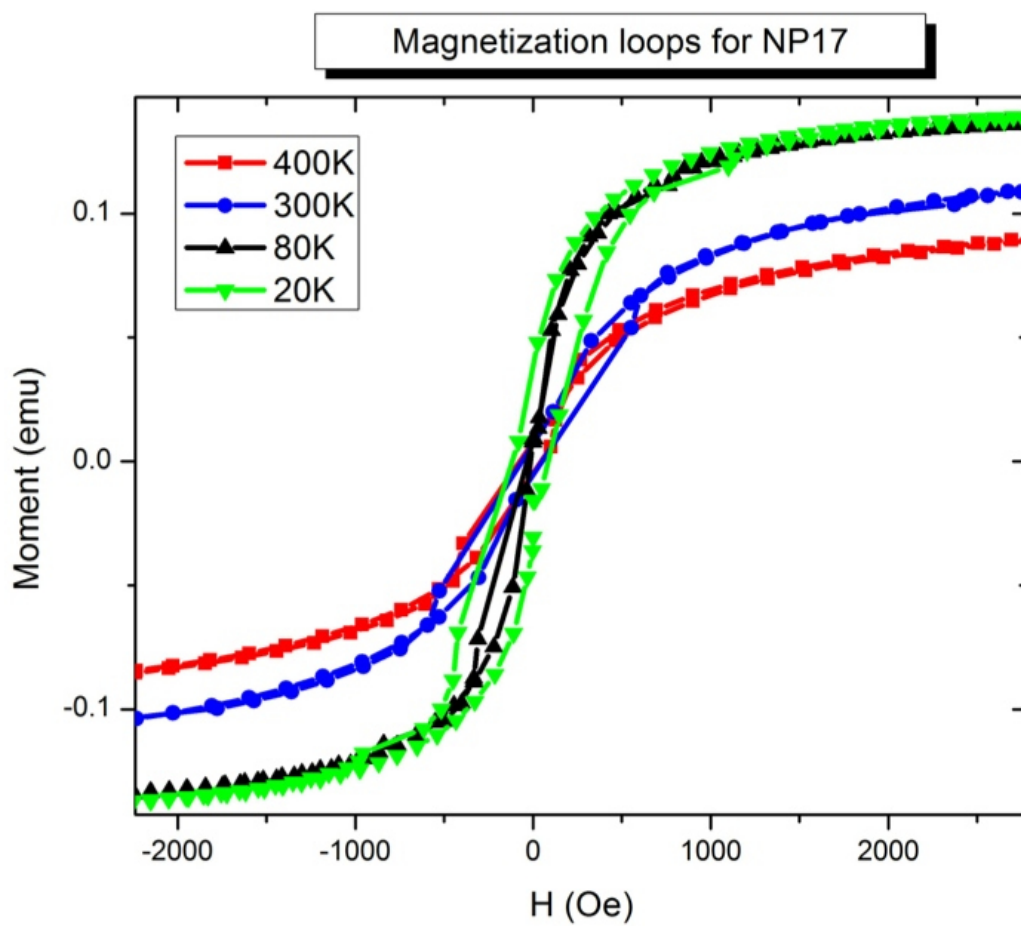
Figure 2.3 Hysterisis effect of sample NP17 at 20 K, 80 K, 300 K and 400 K.
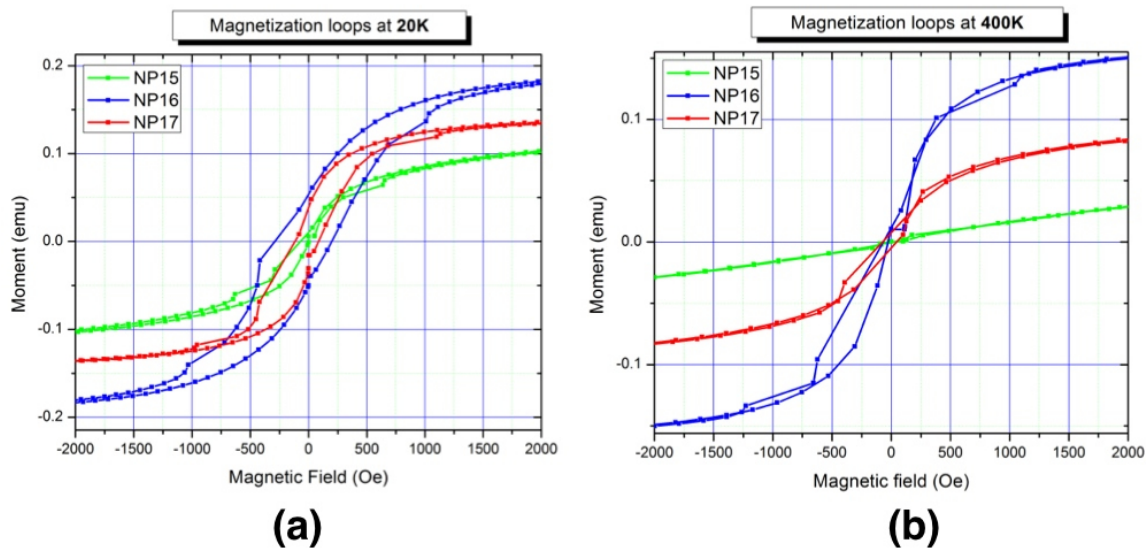
Figure 2.4 Hysteresis effect of sample NP15, NP16 and NP17 at 20 K and 400 K.

T_{join} point. When comparing the FC and ZFC curves, it appears that they do not join at T_{max} but at a higher temperature, indicated by T_{join} on the graph. The gap ΔT between T_{max} and T_{join} is on the order of 100 K for sample NP17, indicating strong magnetic couplings between the nanoparticles.

Magnetization loops, and ZFC / FC measurements were recorded for the three samples. The NP15 comparative plot of ZFC / FC curves measured at 100 Oe, shown in Figure 2.6, clearly shows that the magnetic response of the nanoparticle drastically changes with the particle size. The smaller particles, sample NP15, exhibit a much lower blocking temperature compared to the larger particles, sample NP16. As reported in Table 2.3, T_{max} increases from 28 K for the 5 nm particles up to 170 K for the 11 nm particles that are just twice the size. Also it appears that the joining point for the ZFC / FC curves is much closer to the maximum, only about 10 K above T_{max} for the 5 nm particles, while it increases to about 100 K for the 8 nm and at least 50 K for the 11 nm particles. (The joining point, being arbitrarily defined here, is when the gap between the FC and ZFC curves is reduced to about 10% of the value at the peak.) The increase of the gap
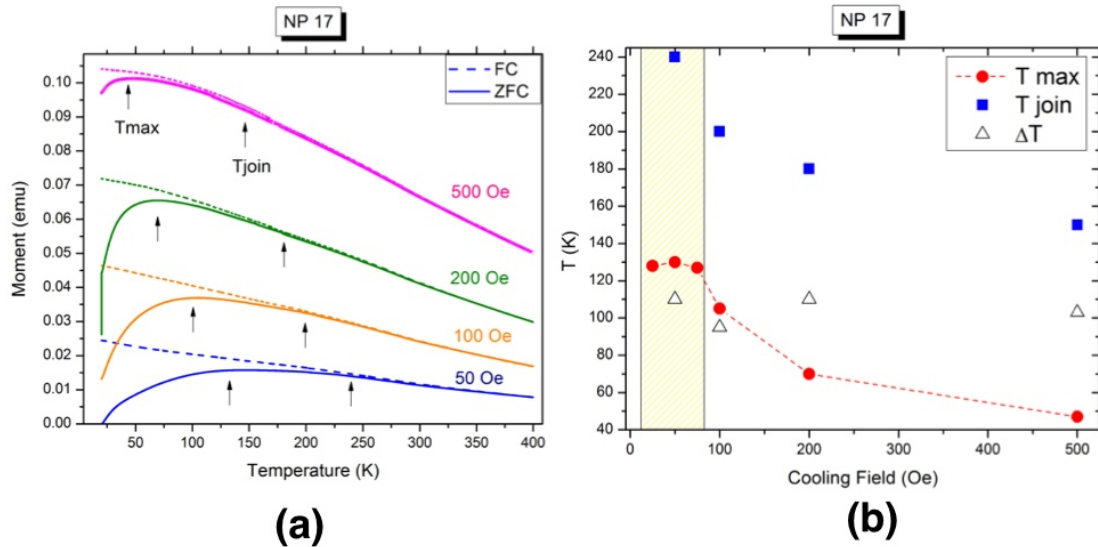
Figure 2.5 (a) ZFC / FC measurements of sample NP17 (8 nm) at 50, 100, 200 and 500 Oe. (b) Graphs of T_{max} and T_{join} as functions of cooling field value

$\Delta T = T_{\text{join}} - T_{\text{max}}$ as particle size increases, indicates that dipolar couplings are almost negligible in the 5 nm particle assemblies, and become much stronger in the larger 8 and 11 nm particles assemblies. Smaller particles carry lower magnetic moment, which will lead to a weaker dipolar coupling. The coupling strength is also related to the interparticle distance between nanoparticles.

Magnetization loops were measured for the three samples. The comparison of the magnetization curves at 400 K shows that the 5 nm particles require a higher field to be aligned (with $H_{0.95} \sim$ 30,000 Oe) while the 11 nm particles align more easily (with $H_{0.95} \sim$ 9,000 Oe) as shown in Table 2.3. It also appears that the 5 nm particles do not exhibit any hysteresis at 400 K, indicating a pure superparamagnetic behaviour, while the larger particles exhibit a small hysteresis, indicating some ferromagnetic-like contribution, due to the strong dipolar couplings. The comparison of the curves at 20 K shows a similar trend although not as drastic, with $H_{0.95} \sim$ 14,000 Oe for the 5 nm particles and $H_{0.95} \sim$ 4000 Oe for the 8 nm particles and $H_{0.95} \sim$ 10,000 Oe basically unchanged for the 11 nm particles. Also the magnetization loops show a very small coercivity H_c on the order

Table 2.3 Structural and Magnetic parameters for samples NP16, 17 and 18.

	Particle size		ZFC/FC curves		Magnetization loops			
	TEM	XRD	$T_{\max}$	ΔT^1	H_c400K	H_c20K	$H_{0.95}400K^2$	$H_{0.95}at20K$
	(nm)	(nm)	(K)	(K)	(Oe)	(Oe)	(Oe)	(Oe)
NP16	5.3 ± 0.7	5.8 ± 1.7	28	∼10	∼0	∼25	29575	14200
NP17	8.1 ± 1.7	8.5 ± 2.9	130	∼100	∼20	105	13100	3900
NP18	11.3 ± 2.5	11.0 ± 4.6	170	∼50	50	235	9145	10272

of 25 Oe for the 5 nm particles, and an increased hysteresis of 100 Oe and 235 Oe for the 8 and 11 nm particles, respectively. The occurrence and amplification of the hysteresis indicate a blocked state at 20 K, with strong magnetic couplings between the particles.

2.4 Discussion

The magnetic behavior of our 5 to 11 nm Fe_3O_4 nanoparticles agrees with magnetic data measured on other Fe_3O_4 nanoparticles by other groups. [17–19] There has been a question about surface effects on the magnetic properties of Fe_3O_4 nanoparticles, when comparing them to Fe_3O_4 bulk properties. One model predicts that the effective magnetic anisotropy K_v of the nanoparticles should be somewhat higher than K_v in the bulk material because of the increased surface to volume ratio. [20] Consequently, it predicts that the coercive field H_c, observed at low temperature, would drastically increase as the particle size decreases. [21] In our case, we found that the coercive field H_c measured at 20 K, actually increases from about 25 Oe to 235 Oe when the particle size

---

[1] ΔT is the difference between $T_{\max}$ and the joining point for the ZFC and FC curves (above $T_{\max}$).

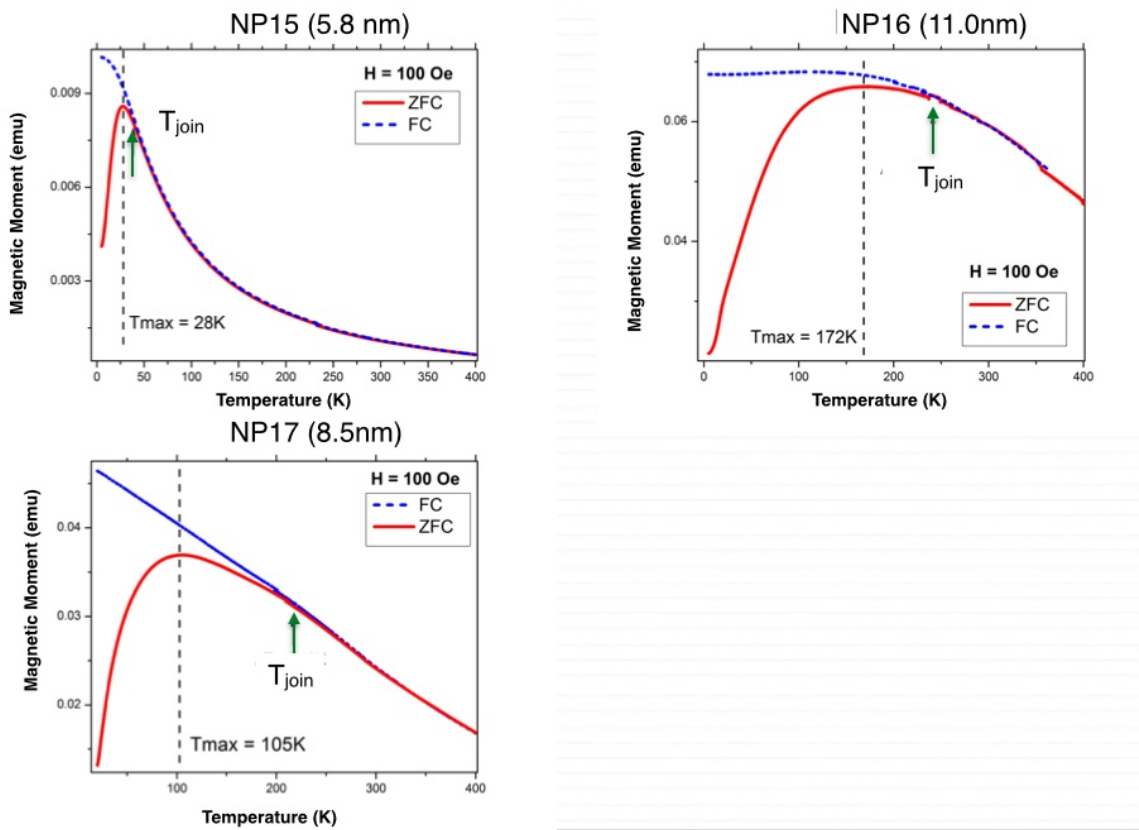[2] H_s is measured at the shoulder of the magnetization curve, preceding saturation.

Figure 2.6 ZFC / FC measurements of sample NP15 (5nm), NP17 (8nm) and NP16 (11nm) measured at 100 Oe. T_{max} is the temperature when the magnetic moment of ZFC curve is at the maximum. T_{join} is the temperature when ZFC and FC curves join.

increases from 5 to 11 nm. Similar behavior has been observed by Guardia et al. [22] on 6 to 20 nm nanoparticles coated with oleic acid, yielding coercive fields in the range of 175 Oe to 370 Oe at 5K. Coercive fields at the same order of magnitude were also reported by Gaya *et. al.* [17], who measured a coercive field increasing from about zero to 330 Oe at room temperature, when the Fe_3O_4 particle size increased from 5 nm to 150 nm. The results are slightly different because of the different preparation methods and some experimental errors. These values for the coercive field are consistent with a coherent rotation of single domain particles and an anisotropy constant K_v close to that of Fe_3O_4 bulk. The consistency of the results, obtained on nanoparticles prepared by different methods, suggests that surface spin disorder effects are here strongly reduced by the presence of oleic acid ligands covalently bonded to the surface of the nanoparticles. [22] With an oleic acid coating, the nanoparticles exhibit bulk like magnetic anisotropy.

Our ZFC / FC results, showing that the maximum temperature T_{max}, and consequently the blocking temperature T_B, drastically increase with particle size, also agree with findings published elsewhere. ZFC / FC measurements performed at 50 Oe on other oleic acid coated particles yielded a T_{max} value of 28 K for 6 nm particles, increasing to well above room temperature for 20 nm particles [22], and 35 K for some other 5 nm particles, increasing to 300 K for 14 nm particles. [23] Other ZFC /FC measurements performed at 500 Oe on Fe_3O_4 nanoparticles prepared by inorganic solution methods, showed a T_{max} value of 45 K for 5 nm particles, increasing to 107 K for 10 nm particles and around 300 K for 50 nm particles. [17] Signs of the Verwey transition have been seen on the ZFC curve on larger particle sizes (50 nm and beyond) but not on smaller particles, like ours. The discrepancies between the observed T_{max} values from the various measurements may be in part due to the differences in the magnitude of the external field applied during the cooling/heating process. But some discrepancies are also observed between data recorded at the same external field values, indicating that the blocking temperature may not only depend on the particle size, but also on the particle preparation and the particle chemical environment during the measurement. The

different published values tend nevertheless to all show that the blocking temperature is essentially controlled by the particle size, being in the range of 30 K for 5 nm particles, and increases very rapidly when the particle size increases, at the nanometric scale, reaching room temperature when sizes approach the 20 -50 nm range. Also, our observations of increased magnetic couplings, where $T_{\text{join}} > T_{\text{max}}$, for larger particles is somewhat consistent with some other measurements. It has been observed on other nanoparticles of 10 nm in size and beyond that $T_{\text{join}} > T_{\text{max}}$ [17] suggesting the presence of aggregates of nanoparticles, where magnetic domains are strongly coupled. Within such aggregates, the giant magnetic moments carried by each particle are randomly aligned in the absence of field (ZFC), but are aligned and strongly coupled in the presence of field (FC). It then requires heating the sample at higher temperatures above the nanoparticle blocking temperature, in order to retrieve the same magnetic response after zero-field-cooling or field-cooling the particles.

Chapter 3

X-ray Magnetic Circular Dichroism (XMCD)

3.1   Overview of the XMCD technique

X-ray absorption spectroscopy (XAS) is a technique for determining the local geometric and electronic structure of materials. It uses a transmission setup as shown in Figure 3.1 to measure the absorption cross-section of given materials. As an extension of XAS, the X-ray Magnetic Circular Dichorism (XMCD) effect measures the change in absorption cross-section when the helicity of polarized light is switched. XMCD is related to the magneto-optical Kerr effect (MOKE). There is however a difference: MOKE uses visible light to measure the magnetization of a sample, while XMCD uses x-ray, and the energy is tuned to the resonant edges of magnetic material so that it is element-selective. In addition, the photons at these resonant edges can excite a dipole transition from a core state to a valence state. Because the energy of a core state is usually well defined, XMCD can be used to probe the shell state information which relates to the magnetic structure of a sample.
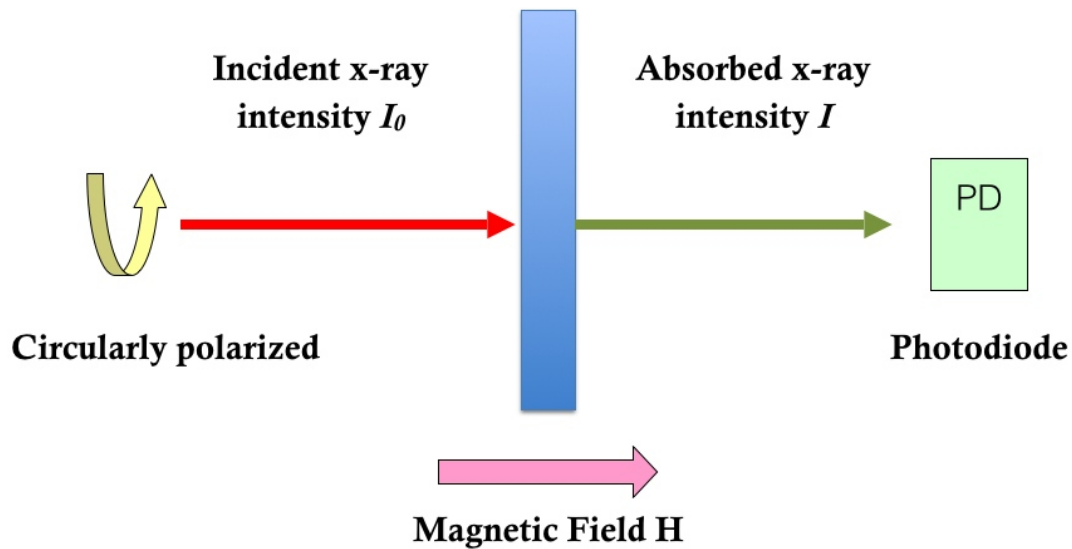
Figure 3.1 Set up of a XAS experiment. The blue rectangular represents the sample.

In 1975, Erskine and Stern [24] first measured a magnetic dichroic effect at the $M_{2,3}$ edges of Ni using circularly polarized x-rays. After about a decade in 1987, the first XMCD experiment was carried out by Schütz *et al* [25] at the *K* edge of Fe.

In our experiment, we utilized the $L_{2,3}$ resonant edges of Fe, which corresponds to the dipole transitions from $2p$ band to $3d$ band. The $2p$ band splits into the $2p_{3/2}(l+s)$ and $2p_{1/2}(l-s)$ energy levels because of the spin-orbit coupling. As a result, the split yields the L_2 and L_3 edges. As illustrated in Figure 3.2, the hole density of states on the $3d$ band is split when the sample is magnetized. When the light is shone onto the sample, the angular momentum carried by the photon is transfered to the electrons in the $2p$ core band. Those photoelectrons will be excited to the holes in the $3d$ band, conserving their spin. Because of the density of states difference between spin up and spin down holes in the $3d$ band, the absorption of left and right polarized x-rays will be different.
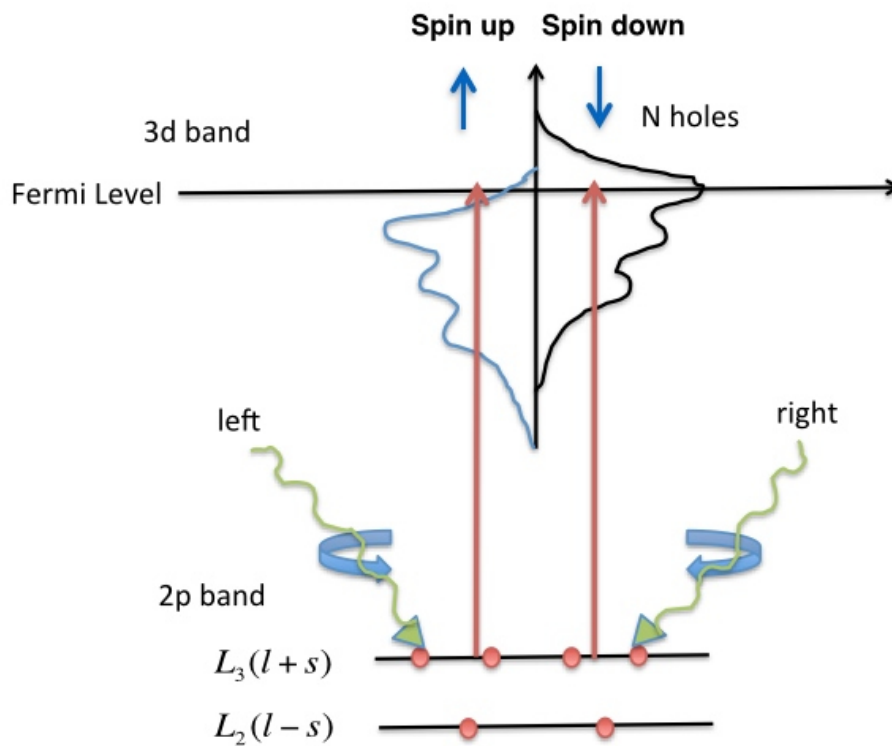
Figure 3.2 An illustration of the dichroic effect for a $2p$ to $3d$ dipole transition in a magnetic material. The red tiny spheres represent the electrons. The red arrows refer to the transition of electrons from $2p$ to $3d$ band. The green curves with blue arrows on it denote the x-ray with left / right polarizations. L_3 and L_2 are the resonant edges of Fe with total angular momentum quantum number $l+s$ and $l-s$, respectively

3.2   Experimental setup

We carried out our XAS measurements at beamline 13-3 of the Stanford Synchrotron Radiation Lightsource (SSRL), at the Stanford Linear Accelerator Center (SLAC). We used circularly polarized soft x-ray light, produced by an elliptical polarization undulator, with a degree of polarization of 98%. The light was finely tuned to the $L_{2,3}$ absorption edges of Fe, using a 1100 l/mm spherical grating monochromator with an energy resolution of 0.2 eV around 700 eV. For this measurement, the Fe_3O_4 nanoparticles were deposited on 50 nm thick Si_3N_4 membranes, with a window size of $100 \times 100 \, \mu$m. The membranes were mounted in transmission geometry onto a cryogenic sample holder in a vacuum chamber. The size of the beam at the location of the sample was about 220 μm $\times$ 70 μm, thus illuminating most of the window and providing fairly good statistics. As illustrated in Figure 3.3, a magnetic field was applied in-situ, in the direction parallel to the beam and perpendicular to the membranes, up to 6.3 kOe. X-ray absorption spectroscopy (XAS) spectra were measured by scanning the energy across the Fe $L_{3,2}$ edges, from 690 eV to 735 eV. To extract the XMCD signal, we divided the transmitted signal I by the incident-photon flux I_0. The transmission signal $T = I/I_0$ shown in Figure 3.4(a) was converted to an absorption cross-section $\mu = -\ln(T)$ displayed in Figure 3.4(b).

We have carefully normalized our absorption spectra in a way that I will explain below. As we can see from the raw absorption spectrum in Figure 3.5, there is a slope in the background. This background slope is due to the charge absorption. One can also notice that the slope for $E < L_3$ (below L_3 edge) is different than slope $E > L_2$ (above L_2 edge). We first subtracted a slope for the whole spectrum and obtained the green curve shown in Figure 3.5. Second, because the charge absorption below and above the $L_{3,2}$ edges are slightly different, it is also necessary to subtract another slope for the data around the L_2 edge and above. The result is displayed in Figure 3.5. Third, we normalized the absorption edge jump to 1, as shown in Figure 3.6. The last step consists of subtracting a two-step function corresponding to removing the $L_{2,3}$ absorption edge jumps, as
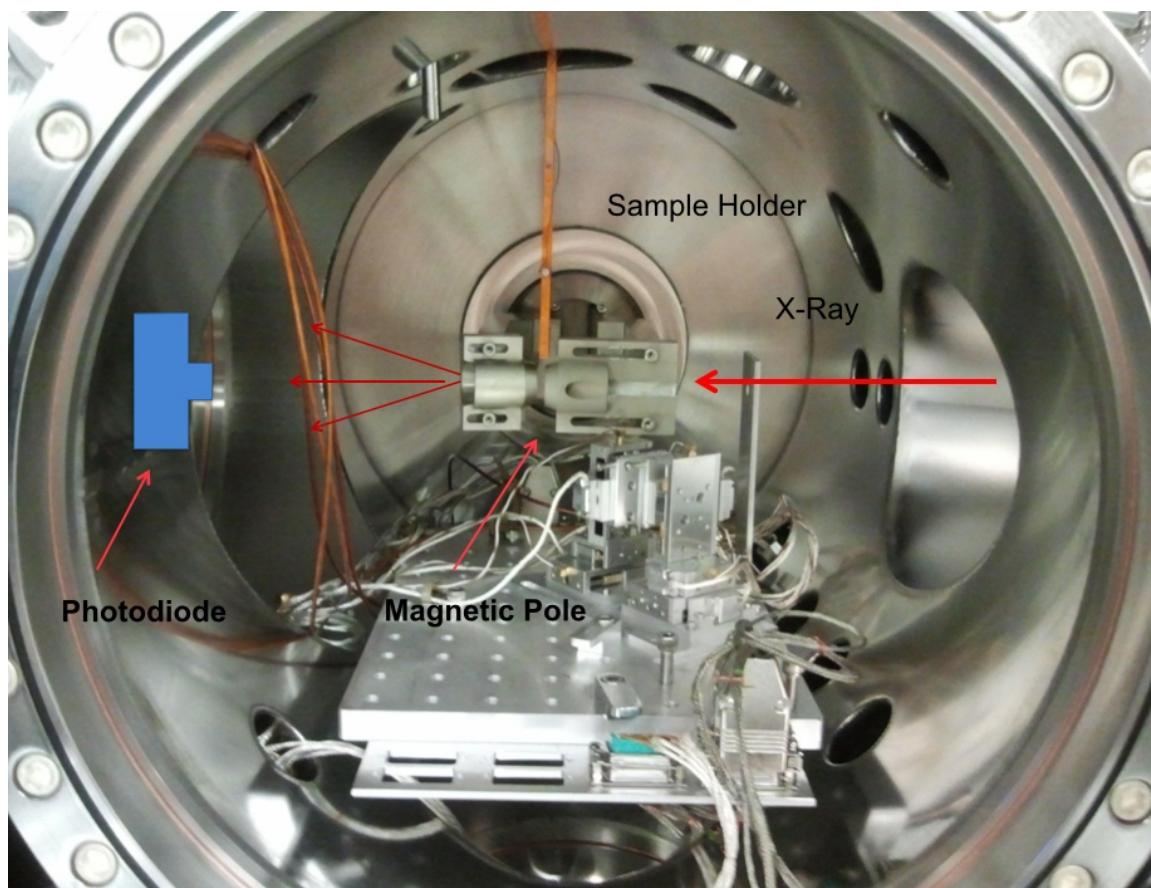
Figure 3.3 View of the scattering chamber used for the XAS/XMCD measurement. X-ray comes from the upstream right side. The sample is mounted on a cryogenic sample holder. A photodiode on downstream side is used to measure the absorption photon flux after x-ray is absorbed by the sample.
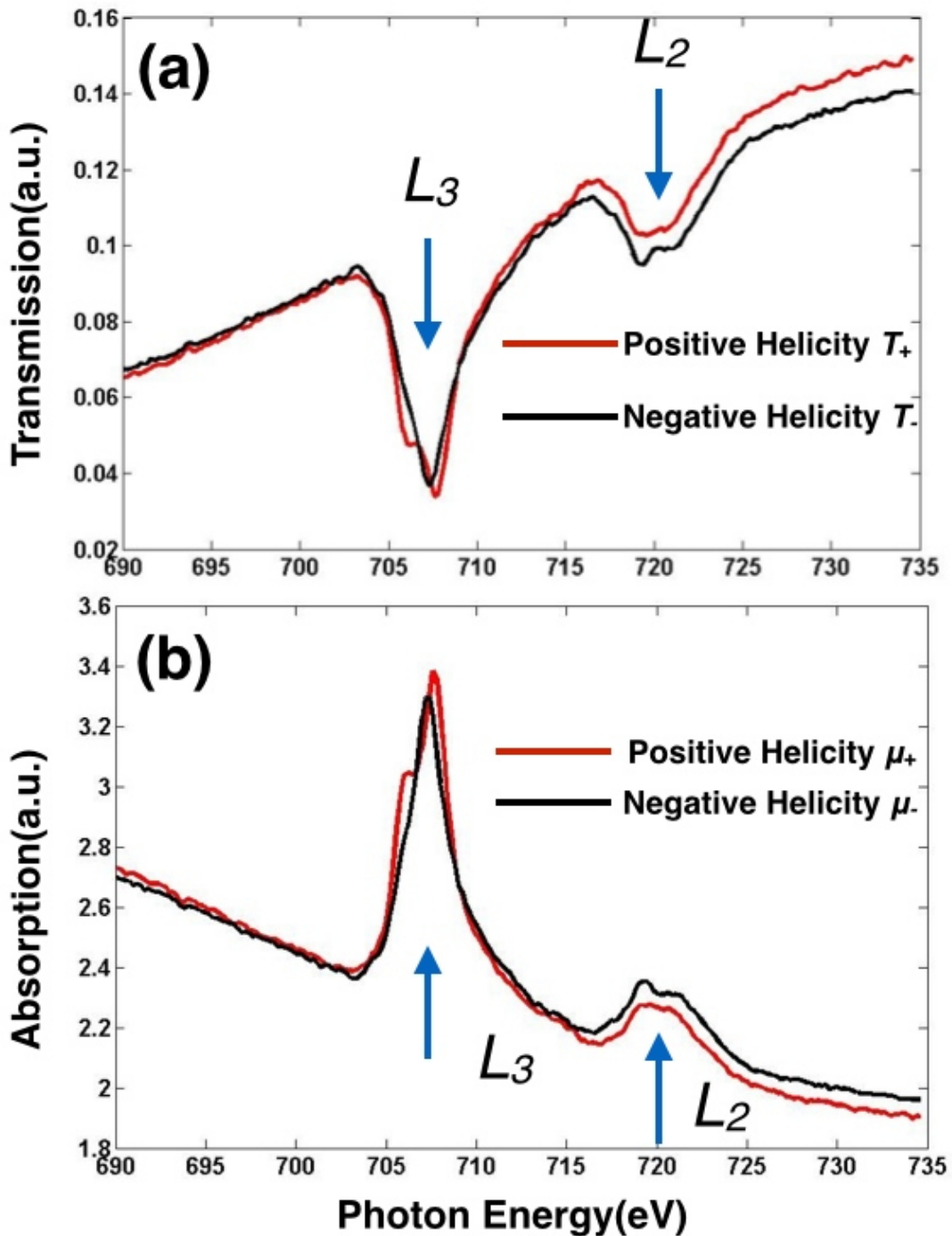
Figure 3.4 (a) X-ray transmission spectrum of NP17 at 300 K measured by XAS. The energy ranges from 690 eV to 735 eV. The field applied on the sample is 6.3 kG. The L_3 and L_2 edges are indicated by blue arrows. (b) X-ray absorption spectrum calculated from the transmission spectrum of NP17 at 300 K. The L_3 and L_2 edges are at the same positions.

also shown in Figure 3.6. [26] One big question that arises here is: for what energy range should we subtract the slope in the second step? We call the lower end of the range the cut-off energy E_c. As we can see in Figure 3.6, if we do not choose the right cut-off energy E_c, the floor between the L_3 and L_2 edges can be lower than the step function. This is not physical, as it would lead to negative absorption. In addition, the choice of cut-off energies also impacts the resulting estimation of orbital and spin moments when using the sum rules. Considering all these issues, we optimized the cut off energy to 719 eV for this set of XAS data.

After the XAS absorption spectra were finely normalized, a XMCD signal was obtained by subtracting the normalized μ_+ and μ_- signals measured at opposite helicities. We show the absorption spectra μ_+ and μ_- and the difference $\mu_- - \mu_+$ of NP17 in Figure 3.7.

In Figure 3.7(b), we can identify a W shape with three peaks in the XMCD spectrum. Two negative peaks (A and C in the figure) correspond to Fe^{2+} and Fe^{3+} ions both in octahedrally-coordinated sites. The positive peak (B in the figure) corresponds to the Fe^{3+} ion in tetrahedrally-coordinated sites, when the spin is antiparallel to the two previous ion spins. [27] We denote the erergies at these peaks as E_A, E_B and E_C, respectively. In comparison to pure iron, which only shows a single peak at the L_3 edge, this W shape is a signature of iron oxide. In Figure 3.8, we also presented XMCD signals for NP16, NP17 and NP18 at different temperatures. At 80 K, the XMCD signal has a peak maximum at around 1.5 while at 300 K the peak only reaches about 0.5. The XMCD signal is significantly stronger at lower temperature. The W shape also varies with different samples. We can see from Figure 3.8 that sample NP17 has higher A and C peaks than sample NP16 and 18 both at 80 K and 300 K. The W shape of NP16 and 18 are weaker, but the A, B and C peak heights are still slightly different. This can be explained by the fact that different samples probably have different degrees of oxidation. Because of that, Fe ions at each site may be slightly different than the theoretical number. Also, our energy step size is only 0.2 eV and the
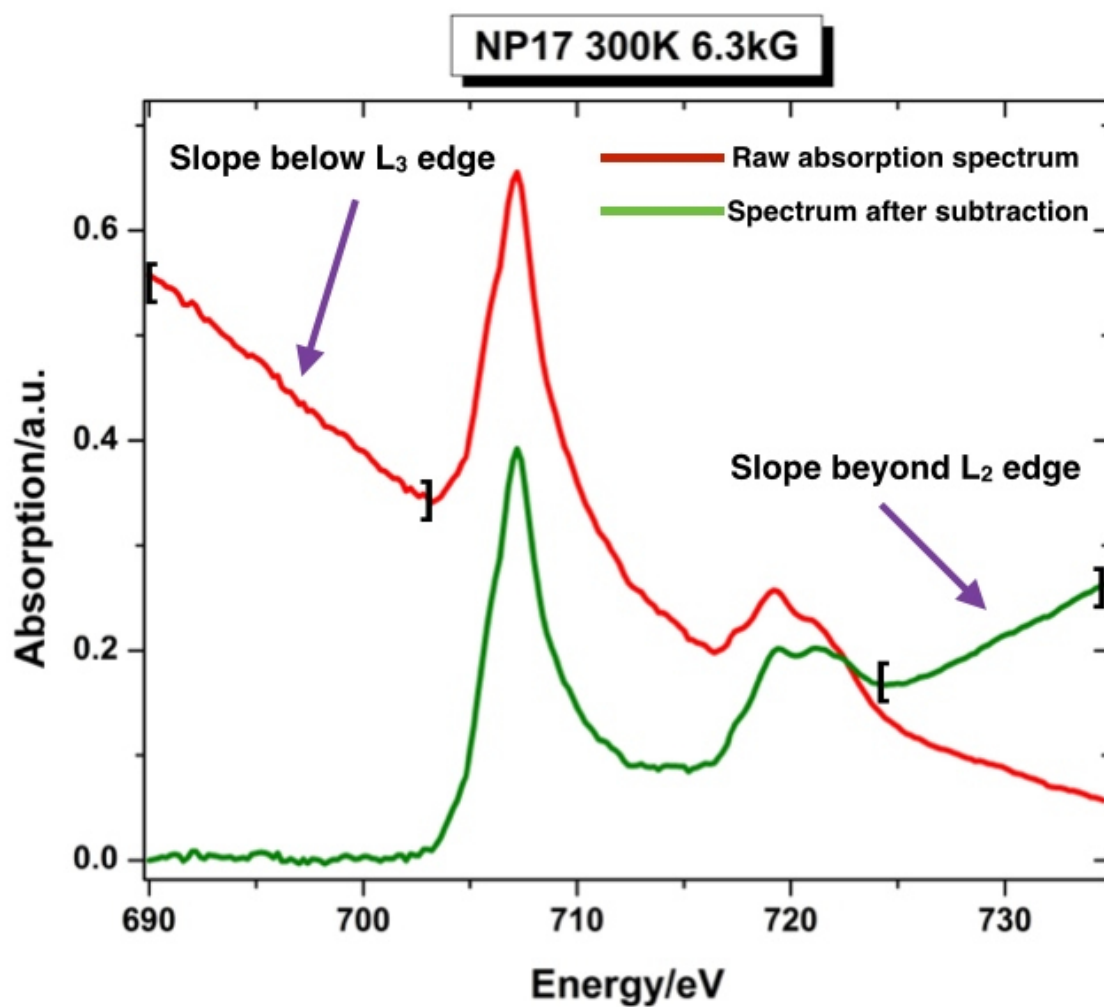
Figure 3.5 Normalization of the XAS absorption signal, step 1. The red curve is the raw absorption spectrum. The background slope can be found by fitting the data below L_3 edge. The green curve is the spectrum after the subtraction, showing another slope beyond L_2 edge. The fiting range of two slopes are indicated by the black brackets.
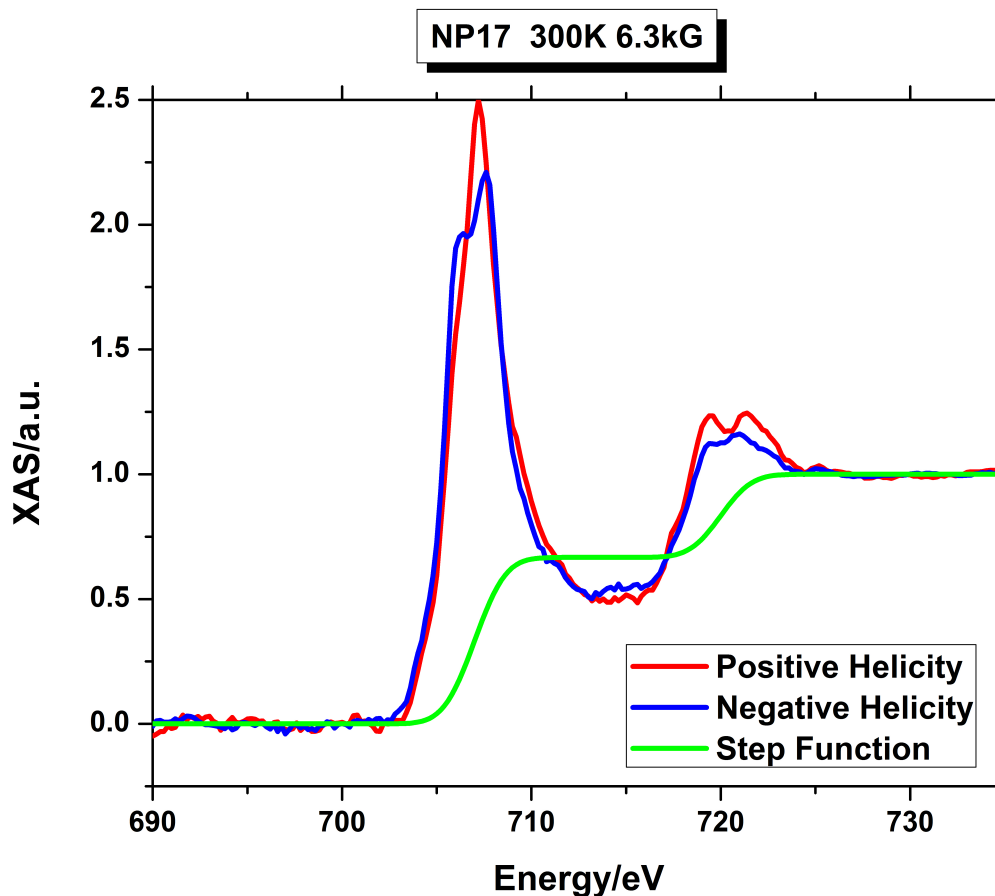
Figure 3.6 Normalization of x-ray absorption signal: step 2. The x-ray absorption edge jump of two absorption spectra with different helicities are normalized to one. The green curve is a simulated two step function. The first step is 2/3 and the second is 1/3 correspond to the different number of electrons on $2p_{3/2}$ and $2p_{1/2}$ energy levels. The first step can be higher than the floor when the cut off energy is not well chosen.
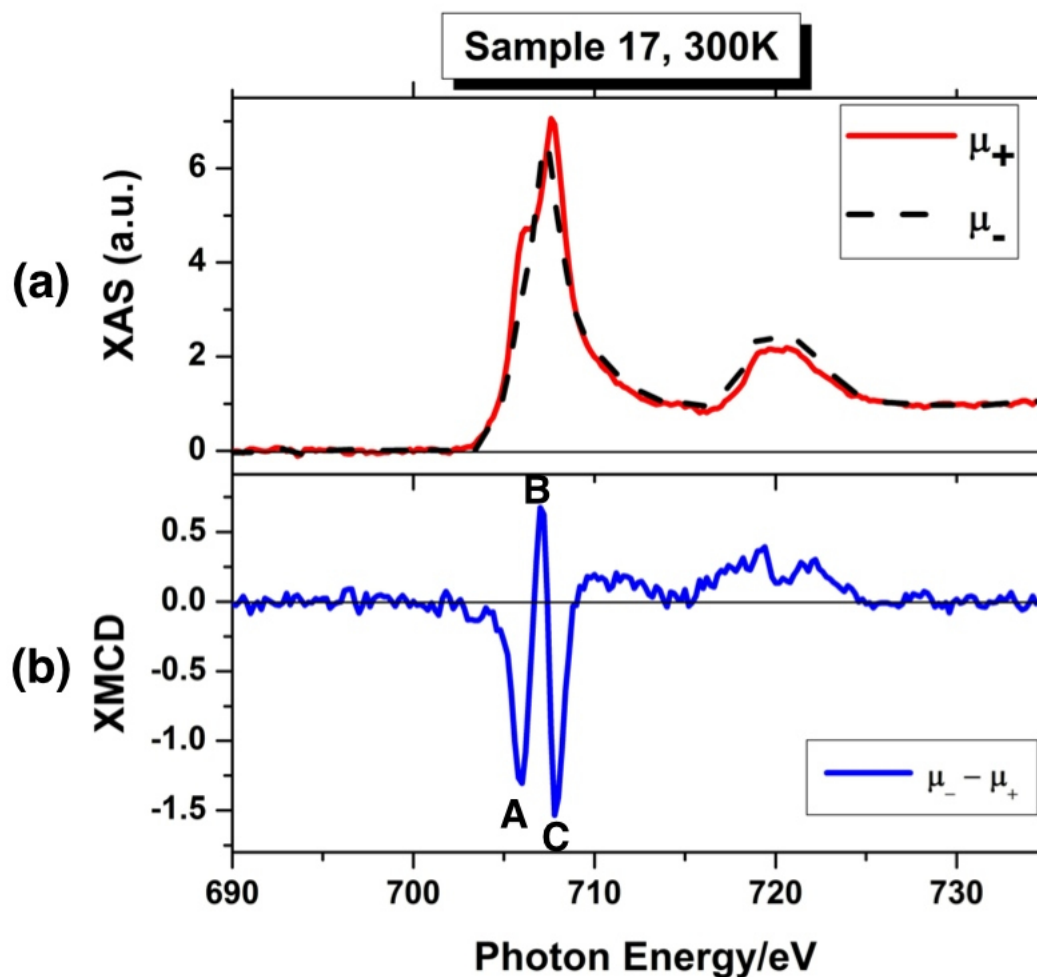
Figure 3.7 (a) X-ray absorption spectra of sample NP17 at 300 K when the helicities of x-ray are positive and negative. (b) XMCD spectrum $\mu_- - \mu_+$ calculated from the x-ray absorption spectra in (a).

peak is very sharp ($\sim$ 1 eV), so we may miss the real peak.

Next, we want to extract the information about the spin and orbital moments of the sample from these XMCD spectra. This is done by using the sum rules, as explained below.
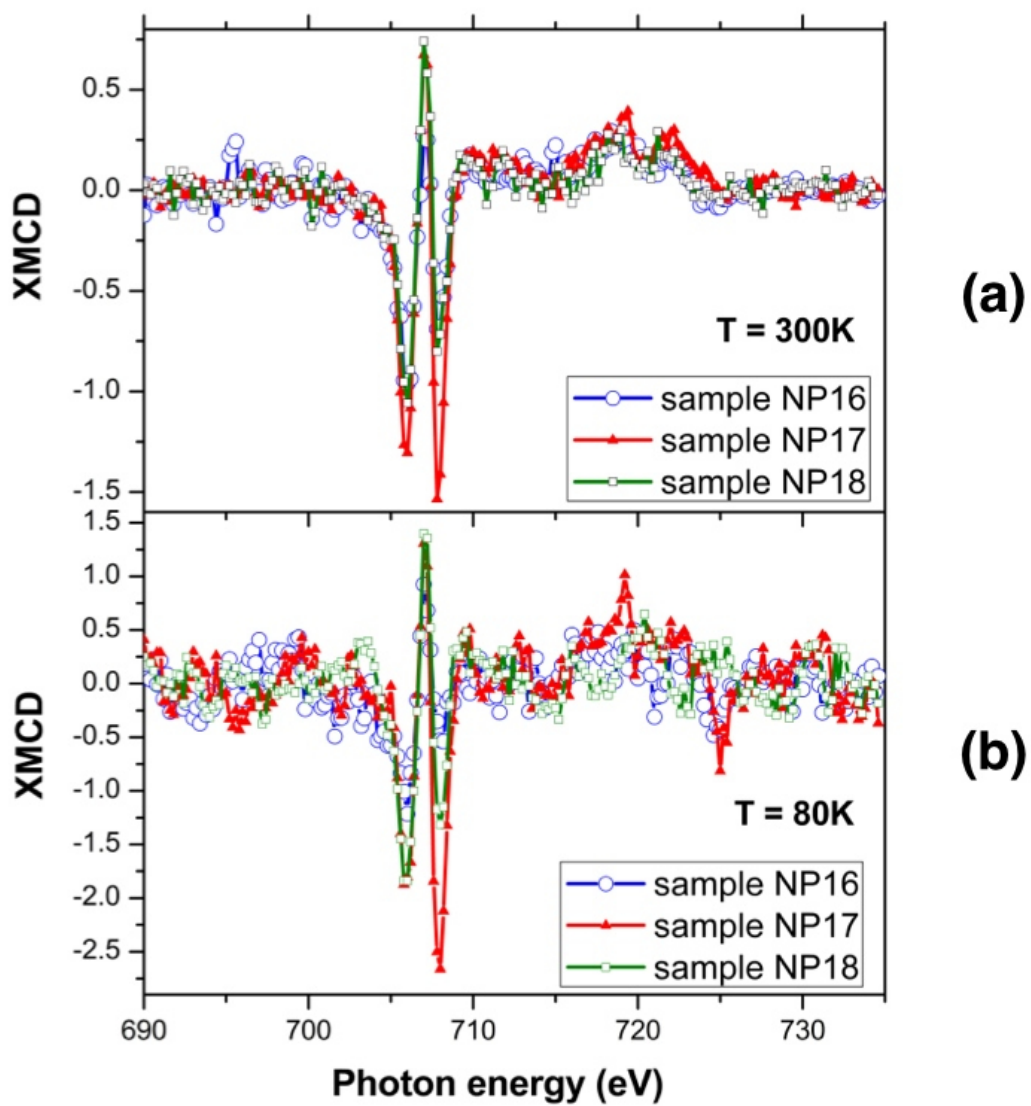
Figure 3.8 (a) XMCD spectra of sample NP16, NP17 and NP18 at 300 K (b) XMCD spectra at 80 K.

3.3   Sum rules

Spin and orbital moments are very important quantities to understand the electronic and magnetic properties of materials. There are formulas called 'sum rules' that allow us to directly extract the spin and orbital moments from XMCD spectra. In 1992, Thole and coworkers [28] developed the sum rules. Since then, people commonly use the sum rules when analyzing XMCD signals in the case of Fe (3d transition metal). The sum rules are:

$$M_L = -\frac{4}{3}\frac{\int_{L_{3,2}}(\mu_+ - \mu_-)d\omega}{\int_{L_{3,2}}(\mu_+ + \mu_-)d\omega}N_h \tag{3.1}$$

$$M_S = -\frac{6\int_{L_3}(\mu_+ - \mu_-)d\omega - 4\int_{L_{3,2}}(\mu_+ - \mu_-)d\omega}{\int_{L_{3,2}}(\mu_+ + \mu_-)d\omega}N_h/(1+\frac{7<T_z>}{2<S_z>}) \tag{3.2}$$

in which M_L and M_S represent the orbital and spin magnetic moments, in units of Bohr magnetons (μ_B). μ_+ and μ_- denote the XAS signal at positive and negative helicities, respectively. $\mu_+ - \mu_-$ is the resulting XMCD signal. ω denotes the photon energy. The integration range is specified for each integral, whether done on the full spectrum ($L_{3,2}$) or through the L_3 edge only (L_3). N_h is the total number of holes in the Fe(3d) valence band, per Fe_3O_4 unit, here $N_h = 13.7$ as reported else where. [29, 30] $<T_z>$ is the expectation value of the magnetic dipole operator. We used a calculated value for $<T_z> = 0.09\mu_B$, as reported elsewhere. [31] S_z is the expectation value for the spin operator, for which we used $<S_z> \cong 4\mu_B$ [32].

We can see from Equation 3.1 that M_L is proportional to the integration of $\mu_- - \mu_+$ (XMCD). We plot the integral of the XMCD spectrum in Figure 3.9 and found that the result at 735 eV is very close to zero. This suggests that we got a quenched orbital moment in our sample.

3.4   Results

Table 3.1 displays the values we calculated for the orbital and spin moments, M_L and M_S, using the sum rules, for three of our samples, at 300 K and 80 K. The moments are here calculated for
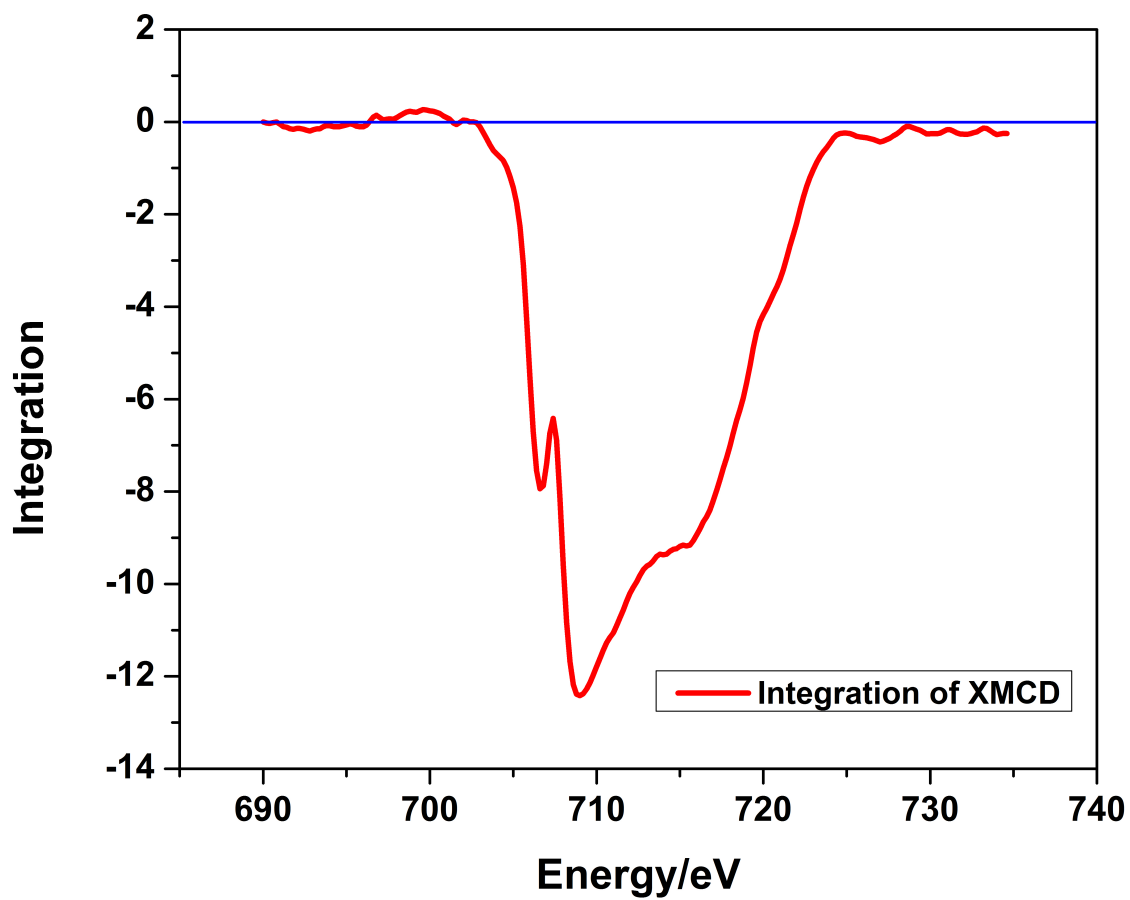
Figure 3.9 The integral of XMCD spectrum over the energy range $695 \sim 735$ eV. M_L is proportional to this integral.

Table 3.1 Calculated values for the orbital and spin contributions to the magnetic moment M_{Fe}

		Values measured at H=6300 Oe[1]						Extrapolated values[2]	
		Orbital $M_L(\mu_B)$		Spin $M_S(\mu_B)$		Total $M_{Fe}(\mu_B)$		Total $M_{Fe}(\mu_B)$	
Sample	Particle size(nm)	300K	80K	300K	80K	300K	80K	300K	80K
NP16	11.3 ± 2.5	0.07(5)	0.06(6)	2.09	2.36	2.16	2.43	2.33	2.57
NP17	8.1 ± 1.7	0.01(5)	0.02(7)	2.26	2.59	2.27	2.62	2.47	2.72
NP18	5.6 ± 1.0	0.03(8)	0.03(7)	1.45	1.70	1.49	1.74	1.91	1.98

the whole unit Fe_3O_4 in Bohr magnetons (μ_B). The net magnetic moment of iron per Fe_3O_4 unit has been estimated by adding the orbital and spin components $M_{Fe} = M_L + M_S$. Also, the XMCD signal was measured at a field of 6.3kOe, which is slightly below saturation point for all samples, therefore the nanoparticles were not fully saturated during the XMCD measurement. We extrapolated M_{Fe} to its value at saturation, using the ratio found in the magnetization curve between the magnetization $M_{6.3kG}$ at 6.3 kOe and magnetization at saturation M_{sat} (estimated at 50000 Oe). The extrapolated values have been obtained by multiplying the measured values by the coefficient $M_{sat}/M_{6.3kG}$. Given the noisiness of the XAS and XMCD data, we believe the error on our estimation of M_s is around $\pm 0.1 \mu_B$.

---

[1]These values are calculated based on a number of hole $N_h = 13.7$.

[2]The values for the total magnetic moment M_{Fe} are extrapolated using the ratio $M_{sat}/M_{0.63T}$ given by the VSM magnetization curves. At 300 K, the ratios are 1.08, 1.09 and 1.28 for NP16, 17 and 18 respectively; at 80 K, the ratios are 1.06, 1.04 and 1.14, respectively.

3.5   Discussion

As shown in Table 3.1, we found quenched orbital moments (M_L) for all the samples at 80 K and 300 K. The values are on the order of 0.01 μ_B. The quenching of the orbital moment is also reported in a theoretical calculation [29] and experimental observations [31] in Fe_3O_4 single crystal. Some other experimental work [27, 33] on Fe_3O_4 nanoparticles have also confirmed a quenched orbital moment. The quenching of the orbital moment appears not affected by the nanostructuration.

We also found a relatively large spin moment (M_S) in our sample as well as the resulting net magnetic moment M_{Fe}. The magnetic field applied on the sample is 6.3 kG, which is slightly less than the saturation field. As reported in the last two columns in Table 3.1, we also extrapolated the total M_{Fe} at saturation. These extrapolated values ($\sim 2\mu_B$) are larger than the values at 6.3 kG, but still somehow lower than the values reported in single bulk Fe_3O_4 ($\sim 3\mu_B$). [29–31] This lowering effect can be explained by a couple of reasons. First, the photon energy range used in our XMCD spectra can be broader. It has been verified that extending the energy range above the L_2 edge yields a larger M_S value. [31] Second, the number of holes $N_h = 13.7$ based on a LDA calculation we used is probably underestimated. The ligand shell around the nanoparticle may modify the electronic structure on the surface, which will increase the number of holes. Third, this lowering effect of the magnetic moment of nanoparticles compared to bulk Fe_3O_4 may also be associated with the nanostructural effect. Last, the oxidation on the surface of the nanoparticles should also be taken into account. As we mentioned in the second chapter, it's very hard to distinguish maghemite (γ-Fe_2O_3) from magnetite (Fe_3O_4). There may be a small portion of maghemite existing in the sample [34].

Chapter 4

X-ray Resonant Magnetic Scattering (XRMS)

4.1   Overview of the XRMS Technique

X-ray diffraction (XRD) probes the crystallographic structure of materials. XRD is typically related to charge scattering, also known as Thomson scattering. X-ray magnetic scattering, a relatively new technique, provides additional information about the magnetic order. The effect was first established theoretically by Platzman and Tzoar [35] and confirmed experimentally by De Bergevin and Brunel [36] in 1970s. In comparison to Thomson scattering, the non-resonant x-ray magnetic scattering amplitude is typically much smaller, down to $\sim 2\%$ [37]. Although magnetic scattering is much weaker than charge scattering, the Resonant X-ray Magnetic Scattering (XRMS) typically has a strong signal, because of magneto optical resonance. XRMS is an element specific technique, in which the scattering amplitude can be drastically enhanced. The first resonant magnetic scattering experiment was reported by Gibbs *et. al.* [37] in 1988. They found a resonant enhancement of the magnetic signal in holmium in which the resonant enhancement reaches a fac-

tor of 50. In the same year, J. P. Hannon and his coworkers [38] proposed a theoretical description of x-ray resonance exchange scattering. These large resonant enhancements can be used to study high-T_c superconductors and two-dimmentional magnetic orderings.

Magnetic scattering is a result of the coupling between the photon spins and electron spins in materials. The resonant enhancement originates from an electric multipole transition. A large enhancement in 3d transition metals at $L_{2,3}$ edges [39] and rare earth $M_{4,5}$ edges [40] has been reported.

Generally, the scattering process can be illustrated as in Figure 4.1, where $\mathbf{k}$ and $\mathbf{k}'$ are the wave vectors of the incident x-rays and the scattered x-rays, respectively. $\mathbf{q} = \mathbf{k}' - \mathbf{k}$ is the scattering vector. We will let $\mathbf{e}$ and $\mathbf{e}'$ represent the polarizations of the incident and scattered x-rays, respectively. The atomic scattering factor is then defined as [41]:

$$f = p_c f_c + p_m f_m \tag{4.1}$$

$$p_c = (\mathbf{e}'^* \cdot \mathbf{e}) \tag{4.2}$$

$$p_m = -i(\mathbf{e}'^* \times \mathbf{e}) \cdot \mathbf{m} \tag{4.3}$$

In Equation 4.1, f_c and f_m denote the complex charge and magnetic scattering amplitudes. p_c and p_m are defined in Equation 4.2 and Equation 4.3, respectively. $\mathbf{m} = \mu/|\mu|$ represents the magnetization direction. In our experiment, we used circular polarization, with small scattering angle θ and $\mathbf{m}$ is longitudinal, along the Z axis. This yields $f_{\pm} \cong f_c \mp i f_m$. [42] The scattering intensity from interfering particles in the Born approximation can be written as:

$$I_{\pm}(q) = |\sum_i f_i e^{i\mathbf{q} \cdot \mathbf{r_i}}|^2 = f_c^2 s_{c\text{-}c}(q) + f_m^2 s_{m\text{-}m}(q) \pm 2 f_c f_m s_{c\text{-}m}(q) \tag{4.4}$$

Where $I_{\pm}$ denotes the scattering intensity of left and right polarized x-rays. i indicates summation over atom i. $s_{c\text{-}c}$, $s_{m\text{-}m}$ and $s_{c\text{-}m}$ refer to the spatial distribution of charge-charge, magnetic-magnetic and charge-magnetic correlations, respectively. In this equation, the first part is a pure charge term, the second one is a pure magnetic term and the last one is a charge magnetic cross term. In our
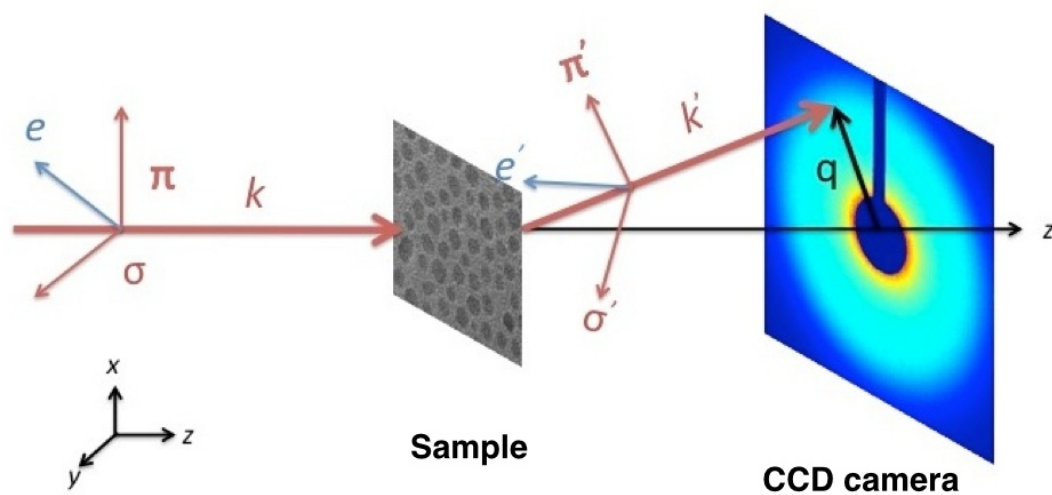
Figure 4.1 Polarized x-ray has a wave vector of **k** and the polarization plane is defined by **e**. The scattered wave vector is **k**′ and the scattered polarization is **e**′. π and σ are the basis vectors in and out of plane for the incident wave. π' and σ' are the basis vectors in and out of plane for the scattered wave.

experiment, we used I_+, I_- and I_{linear} to obtain the charge-magnetic and magnetic-magnetic corre-lations. These correlations can give information on the magnetic coupling between nanoparticles.

In 2005, Kortright *et at* [41] have reported the XRMS using dense assemblies of ε-*Co* and *hcp-Co* superparamagnetic particles using a 1D detector. In our expriment, we studied superparam-agnetic nanoparticles self-assemblies via XRMS, and specifically focused on Fe_3O_4 nanoparticles using a 2D detector.

4.2 Experimental setup

The experimental setup we used at SSRL is shown in Figure 4.2. In our case, we want to probe the magnetism of Fe. We tuned the energy of the x-rays to the L_3 ($\sim$705 eV) and L_2 ($\sim$719 eV) resonant edges of Fe, which correspond to the electric dipole transition from the $2p$ to $3d$ bands of Fe. To perform the XRMS experiment, the photodiode on the downstream side was replaced by a 2048×2048 pixels CCD camera. This camera can be freely adjusted in the X, Y and Z directions to obtain the best data image. By using liquid nitrogen and liquid helium, we were able to cool the scattering chamber down to 20 K. While carrying out the experiment, we set our temperature at 20 K, 80 K, 150 K and 300 K. A picture of the scattering chamber and cooling system is shown in Figure 4.3

The original electromagnet we used at the beamline only produces a magnetic field ranging from -1.1 kG to 1.1 kG. But for our sample, 1.1 kG is far below the saturation field. To increase the magnetic field, we first mounted a permanent magnet onto the magnet poles, which induces a permanent field of $\sim$ 3kG. This magnetic field is already significantly increased but still slightly below the saturation field. Then we managed to implement a electromagnetic inside the chamber by wiring coils around the magnet poles, thus increasing the field further, up to 6.3 kG. Because the scattering chamber is vacuum and the electromagnet releases heat into the chamber, we could
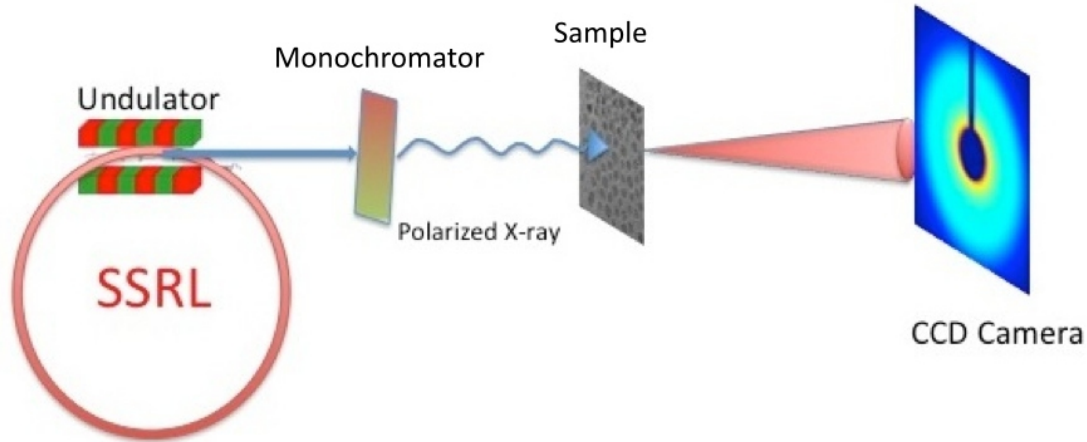
Figure 4.2 Sketch of the XRMS experiment. Coherent x-ray comes from SSRL is polarized by an undulator and tuned to the resonant edges of iron by a monochromater. X-ray is scattered by Fe_3O_4 assemblie and detected by a CCD camera.

not apply a very large current in the electromagnet. However, with the new magnetic setup, we obtained a maximum magnetic field reaching all the way to 6.3 kG *in situ*, which is very close to the saturation field of our samples.

4.3   Experimental results

One of our XRMS scattering patterns is shown in Figure 4.4(a), with colors that indicate different intensities. We identify rings with different intensities by making a set of rings as shown in Figure 4.5. This set of rings share the same center position with the scattering pattern. We can select one ring with a certian radius in the data image by choosing the ring with the same radius in the ring set and multiply the data image by it. The dark lollipop-like shape located in the center is a shadow of a blocker and is used to protect the CCD camera from being hit by direct light. In order
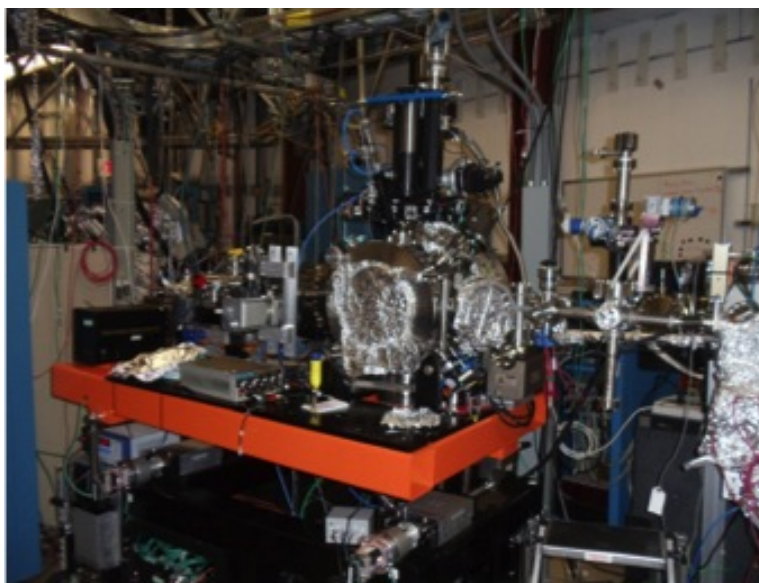
Figure 4.3 View of the scattering chamber used at BL13-3. The scattering chamber has a cylindrical shape. A lot of tin foil are covered around the chamber to protect it from the radiation from outside. The electromagnet is located in the back of the chamber. Detection stage downstream on the left side.

to optimize the data, we tried different configurations.We used different shapes of blockers. For example, a lollipop-like one, a cross-like one, or a simple rod, as shown in Figure 4.6. Also, to access different q regions, we sometimes offset the center of the ring to the right side as displayed in Figure 4.6(a).

To study the scattering pattern, we will generate an intensity profile. To do this, we first have to eliminate the effect of the blocker. The intensity of the pixels within the blocker area is significantly lower than the intensity of the scattering pattern. But when analyzing the data, these 'bad points' will still be counted and on average will reduce the average intensity we obtained for each q value. They may also cause very odd kinks in the intensity profile. Therefore, while analyzing the data, we need to remove the low intensity behind the blocker by multiplying the mask by the image. We developed an algorithm to simulate the blocker and create a mask. Generally, the intensity of the blocker is significantly lower than on the rings. Therefore we set a criterion ε
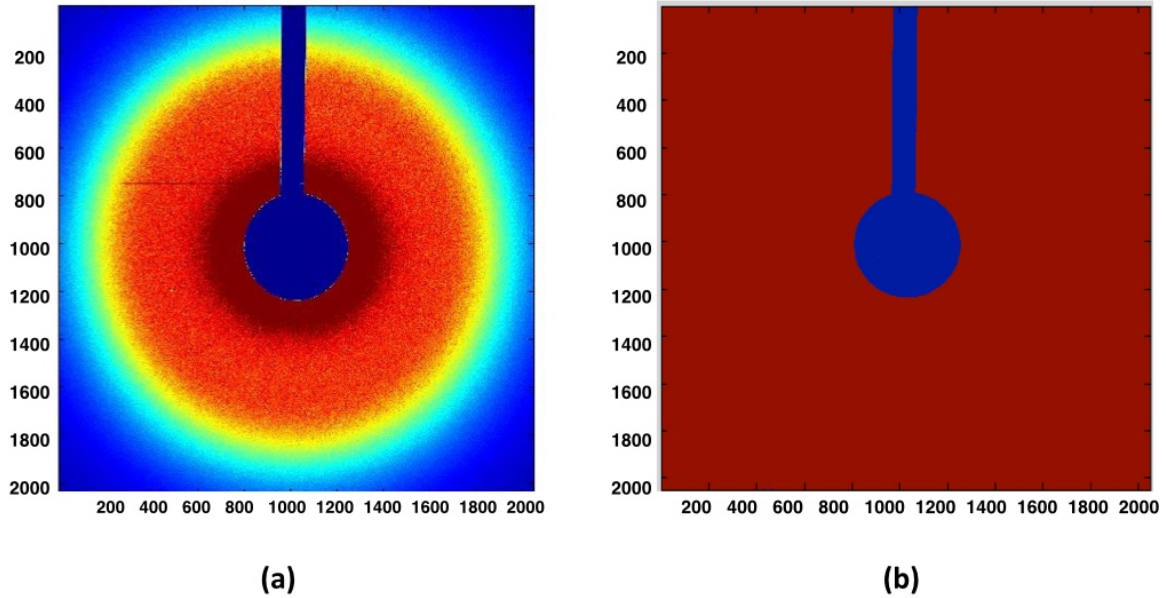
(a)   (b)

Figure 4.4 (a) Scattering pattern measured by the CCD camera from the XRMS experiments. The blue region in the middle is the shadow of the blocker. Red indicates higher intensity, while blue indicates lower intensity. (b) Blocker simulation we used to eliminate the effect of blocker. The blue and red colors have intensity of 1 and 0, respectively

to distinguish the intensity on the blocker from the actual scattering intensity. To do this, we set ε at a certain value. All the pixels that have an intensity lower than ε will be assigned zero and pixels with higher intensity than ε will be assigned 1. The mask corresponding to Figure 4.6(a) is displayed in Figure 4.6(b). It matches the real blocker in the data image very well.

After the shadow of the blocker is removed, we apply two normalization steps to study the scattering pattern. First, we preform a spatial normalization: a single pixel in the scattering pattern does not give us sufficient statistics. Instead, we integrate azimuthally over rings at different q values to generate a intensity profile as a function of q. Second, time normalization: to get rid of the fluctuation of the incident x-rays, we also use a time normalization.

Spatial Normalization   We analyze the data in order to generate an intensity profile of the scattering pattern with respect to q. The scattering factor q is defined in the first section as $\mathbf{q} = \mathbf{k}' - \mathbf{k}$,
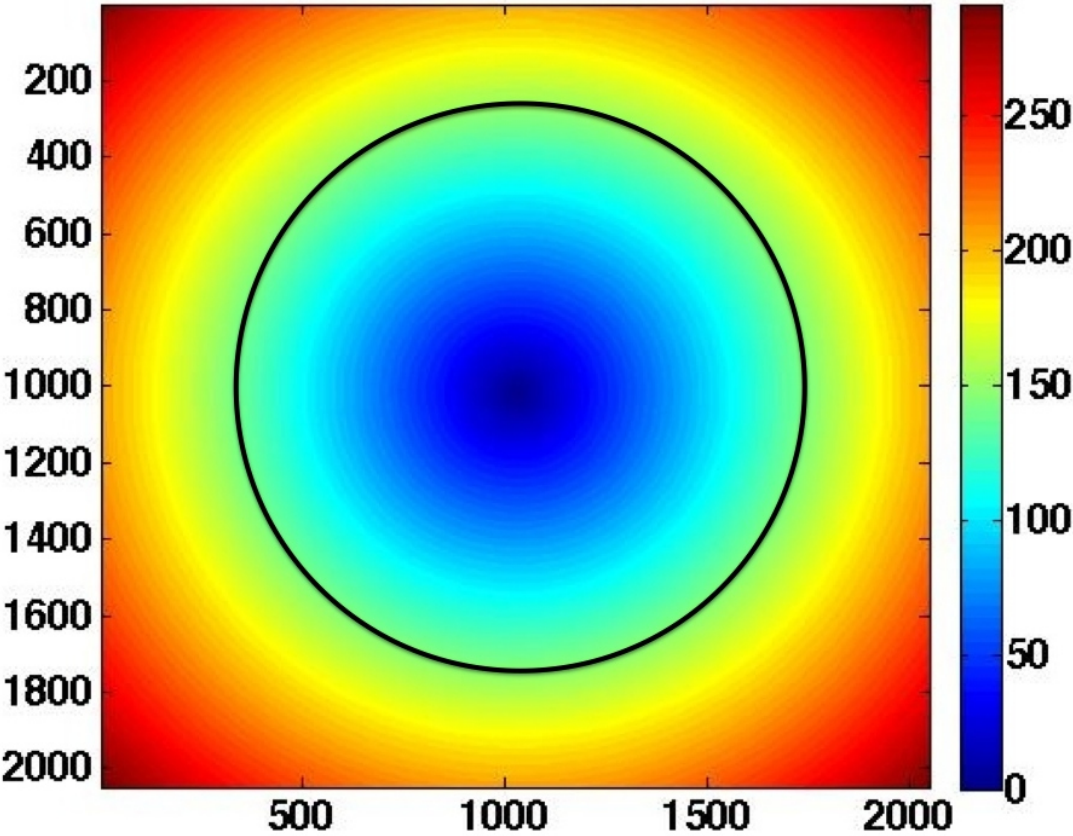
Figure 4.5 A set of rings with different radii. Each ring has a width of 5 pixels. A certain intensity value is assigned to each ring, which is indicated by the colors in the figure.

(a)   (b)

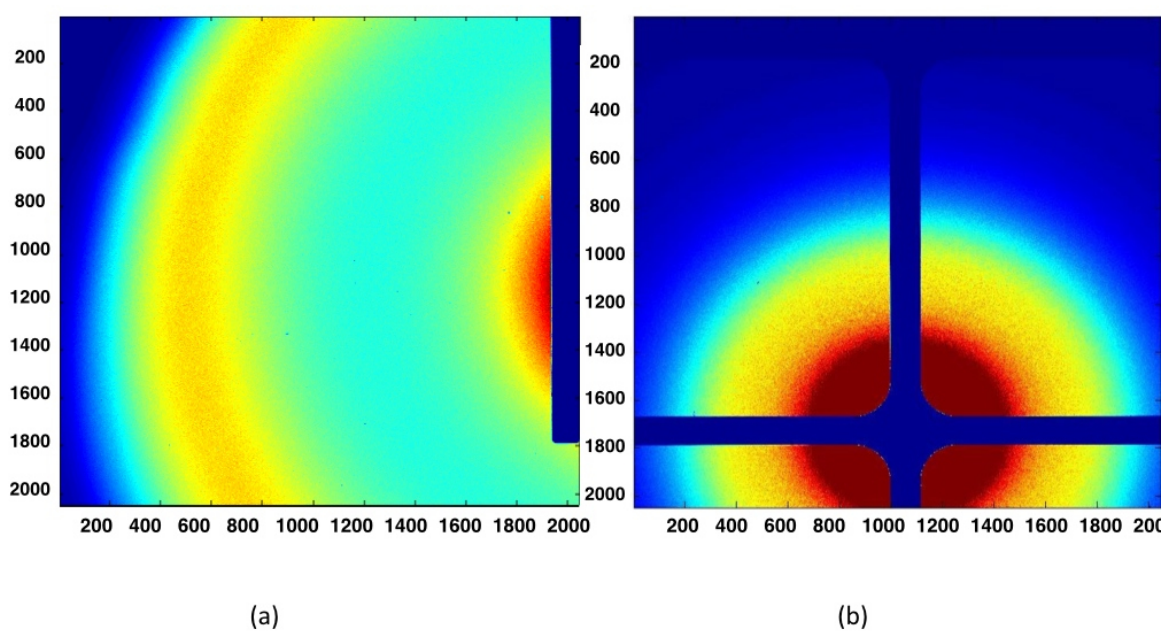**Figure 4.6** (a) The scattering pattern with a simple rod shape blocker. The center is on the right side of the image. We do not have a whole ring here, but we are able to access the larger q value regions with this setup. (b) The scattering pattern with a cross-like blocker. The center of the ring is offset to the bottom. We are also able to access the larger q value regions with this setup.

the difference between scattered wave vector $\mathbf{k}'$ and incident wave vector $\mathbf{k}$ which is also shown in Figure 4.1. The intensity was calculated by an azimuthal integration and normalized by the azimuthal angle θ as illustrated in Figure 4.7(a):

$$I = \frac{\sum\limits_{\Delta\theta} I_{\text{raw}}}{\Delta\theta} \qquad (4.5)$$

In this equation, $\Delta\theta$ is the azimuthal angle of the ring at a certain $\mathbf{q}$ value. It includes all the data points except the ones on the blocker. We numerically calculated the angle by counting the pixel numbers on the ring. I_{raw} denotes the intensity of each pixel on the ring.

Time Normalization The beamline can be unstable due to changes in room temperature and small mechanical vibrations of the facility. Normalizing by the incident x-ray flux time scan is also useful. We call it time normalization I/I_0. The time scan is in Figure 4.7(b). I_0 is the integration of all the peaks in the figure, which correspond to the periods of time when the CCD shutter is open.

4.4   Magnetic profile

Once the spatial normalization and time normalization are done, we are able to plot the scattering intensity profile as a function of q (denoted $I(q)$). We have measured various profiles at different temperatures, energies, and polarizations. In Figure 4.8, we show intensity profiles of sample NP16 and NP18. The intensity profiles have a dominant charge scattering part and a magnetic scattering part. In this figure, the peak position is mostly due to the charge scattering. This peak gives the information about the interparticle distance between two nanoparticles. To determine the distance d, we use the Bragg diffraction condition:

$$q = \frac{2\pi}{\lambda}\sin\theta \qquad (4.6)$$

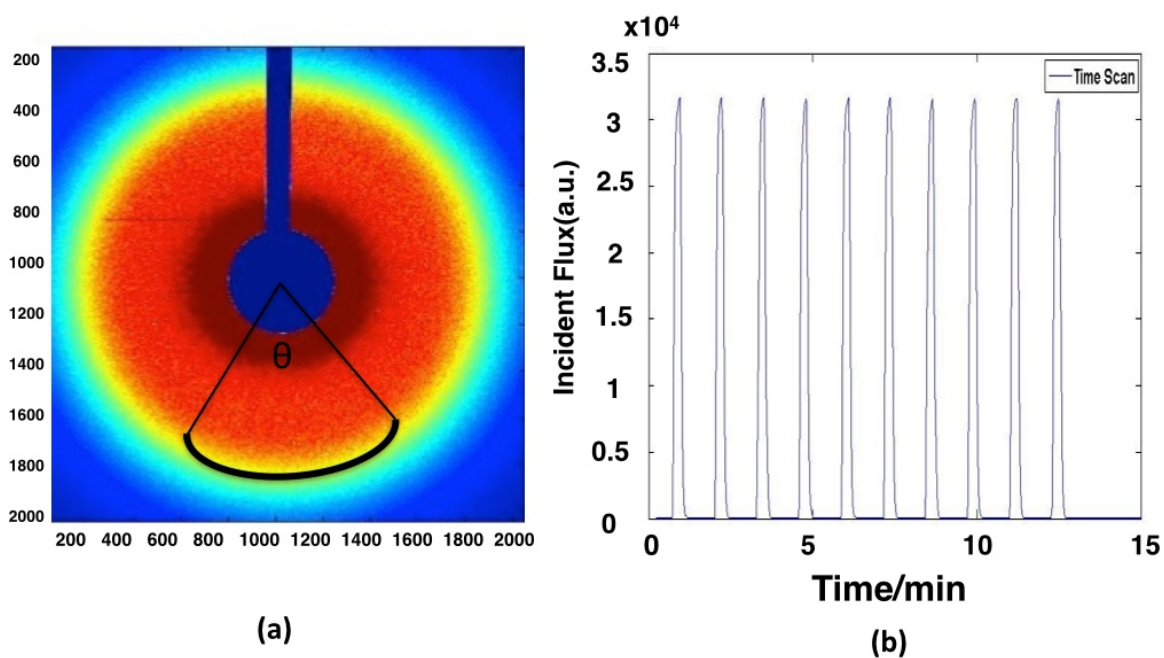$$d = \frac{\lambda}{\sin\theta} = \frac{2\pi}{q} \qquad (4.7)$$

(a)

(b)

Figure 4.7 (a) Illustration of the spatial normalization. We integrated the intensity of each pixel azimuthally and divided it by the azimuthal angle θ. The angle θ is only used to represent the azimuthal angle. The actual azimuthal angle we use is the angle which covers the whole ring except the blocker. (b) Time scan of the incident x-ray flux, each peak indicates the time in between shutter open and shutter close.

where d is the interparticle distance and λ ($\sim$1.76 nm) is the wavelength of the x-ray. We use the first order peak here, so $n = 1$. $\sin\theta = \frac{D}{L}$, where D is the distance from the center of the scattering pattern to each ring and L is the distance between the sample and the CCD camera.

With this equation, we are able to find the interparticle distance of NP16 to be $d = 16.35$nm. In Chapter 2, we found the average size of NP16 is around $a = 11.3$nm. Because nanoparticles are sparsely distributed, the interparticle distance is necessarily larger than the diameter of nanoparticles. There is an average spacing around 5 nm between two nanoparticles. In NP18, we estimated an interparticle distance of around 6.23 nm. It is also consistent with the TEM results, which shows the average size of the nanoparticles to be around $a = 5.6$nm. NP18 has a spacing about 0.6 nm, which indicates that NP18 is more closely-packed than NP16.

We also measured the half peak width to calculate the correlation length of each sample. The correlation lengths are $l_c = 31.57$nm and $l_c = 27.08$nm for NP16 and NP18, respectively. The correlation length indicates that there is only a short range order in NP16, about 2 particles are correlated, while there's a significantly longer range order in NP18, about $4 \sim 5$ particles are correlated.

We also looked at the profile with an energy below the resonant edge. We still choose sample NP16 at 300 K. In Figure 4.9, showing data for NP16 at 300 K, we found the on-resonance intensity profile is one order of magnitude larger than the off-resonant profiles. This is because when the energy is at off-resonance edge, both charge and magnetic scattering are significantly weaker. By studying the peak heights in both Figure 4.9(a) and (b), we found the enhancement at resonance to be at least a factor of 30.

Now we compare profiles taken at different helicities. In Figure 4.10, we presented results of NP16 at 80 K, when a field of 6.3 kG is applied. This figure shows profiles with opposite polarizations at $E_A = 707$eV. We can see from the figure that the intensity profile for a positive helicity is a little lower than for the negative helicity one. We recall Equation 4.4, the charge
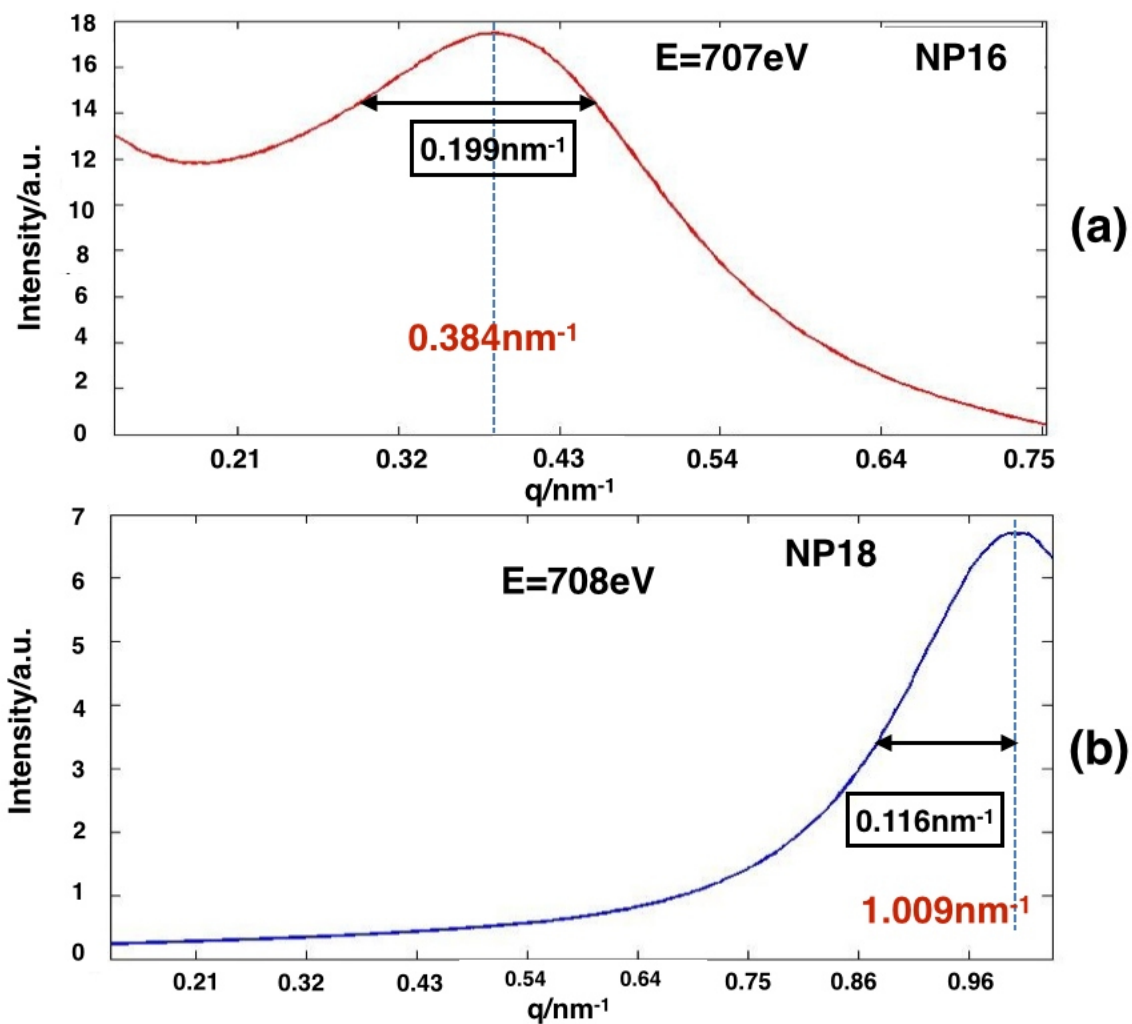
Figure 4.8 (a) Scattering intensity profile respects to q of NP16 (11.3 nm) at 80 K at 6.3 kG. (b) Scattering intensity profile of NP18 (5.6 nm) at 300 K at 2 kG.
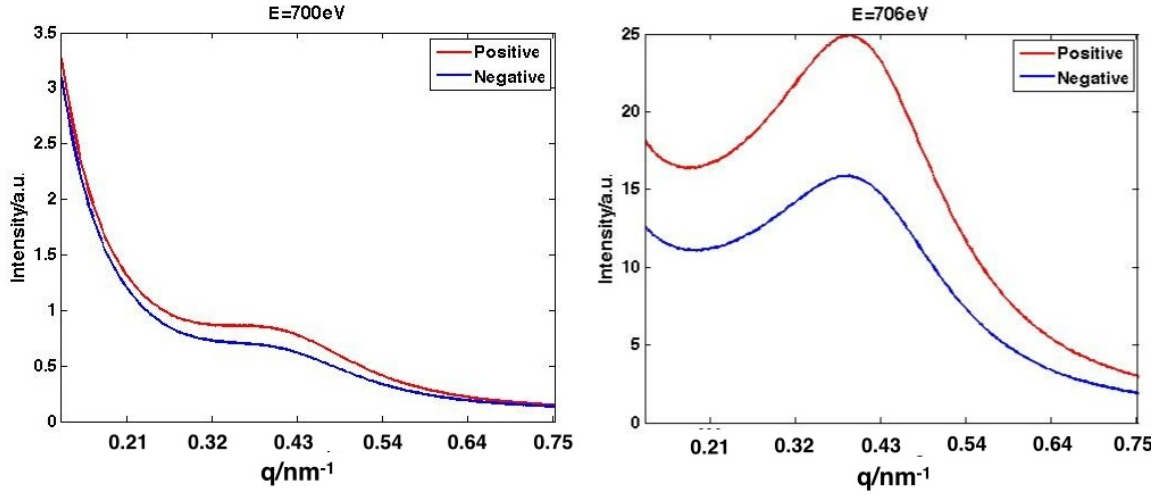
Figure 4.9 (a) Scattering intensity profile of NP16 (11.3 nm) at an below-edge energy 700 eV. (b)Scattering intensity profile of NP16 (11.3 nm) at the resonant edge 706 eV.

scattering term should be independent of the helicity, only the cross term and the pure magnetic term has a dependence on the helicity. Our results indicate the presence of a magnetic scattering signal here. To further study the magnetic scattering signal, we will calculate a dichroic ratio, as shown below.

4.5 Dichroic effect

To extract the charge-magnetic correlation s_{c-m}, we calculated the dichroic term which is defined as:

$$\Delta I(q) = I_+(q) - I_-(q) \tag{4.8}$$

Here I_+ is the scattering intensity profile with positive helicity and I_- is with negative helicity. Using Equation 4.4, we find:

$$\Delta I(q) = I_+(q) - I_-(q) = 2f_c f_m s_{c-m}(q) \tag{4.9}$$
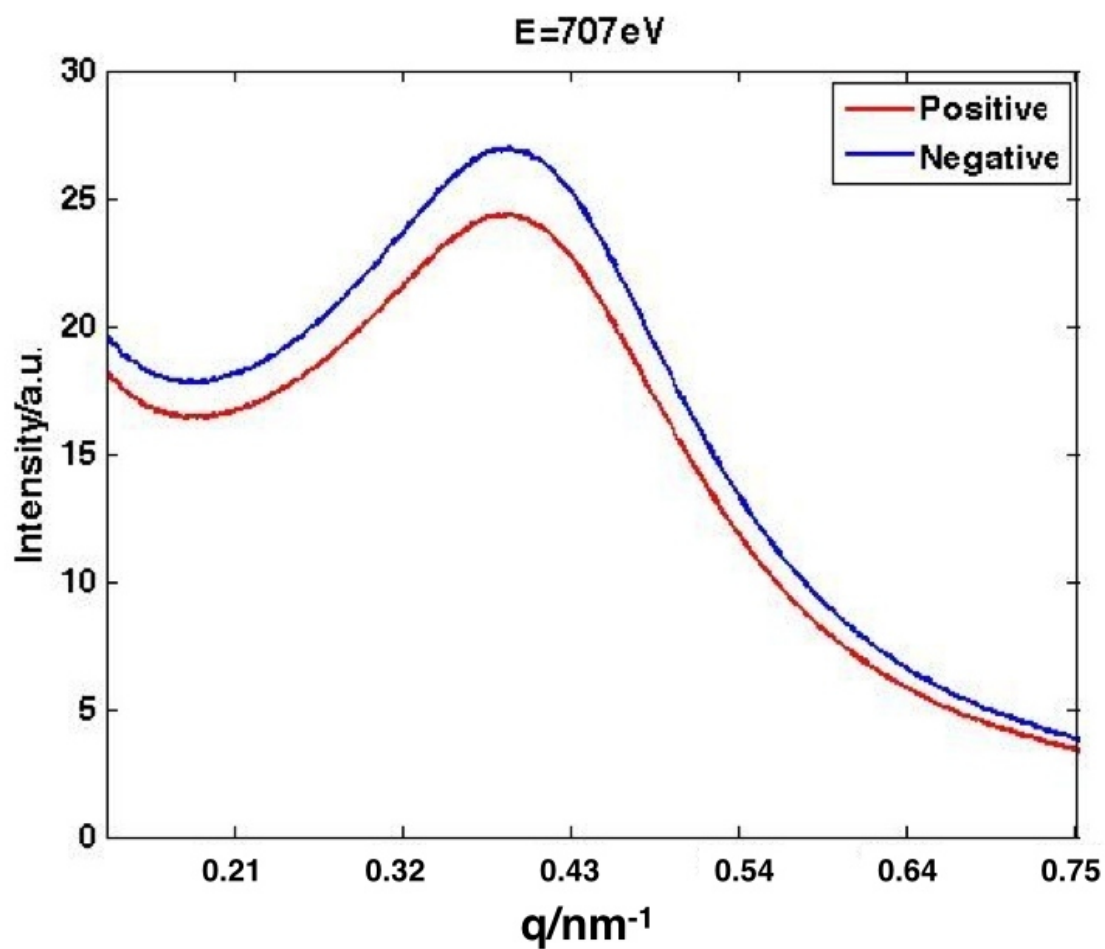
Figure 4.10 Scattering intensity profiles of sample NP16 (11.3 nm) at different helicities at 80 K with a field of 6.3 kG. Different polarizations are indicated by different colors.
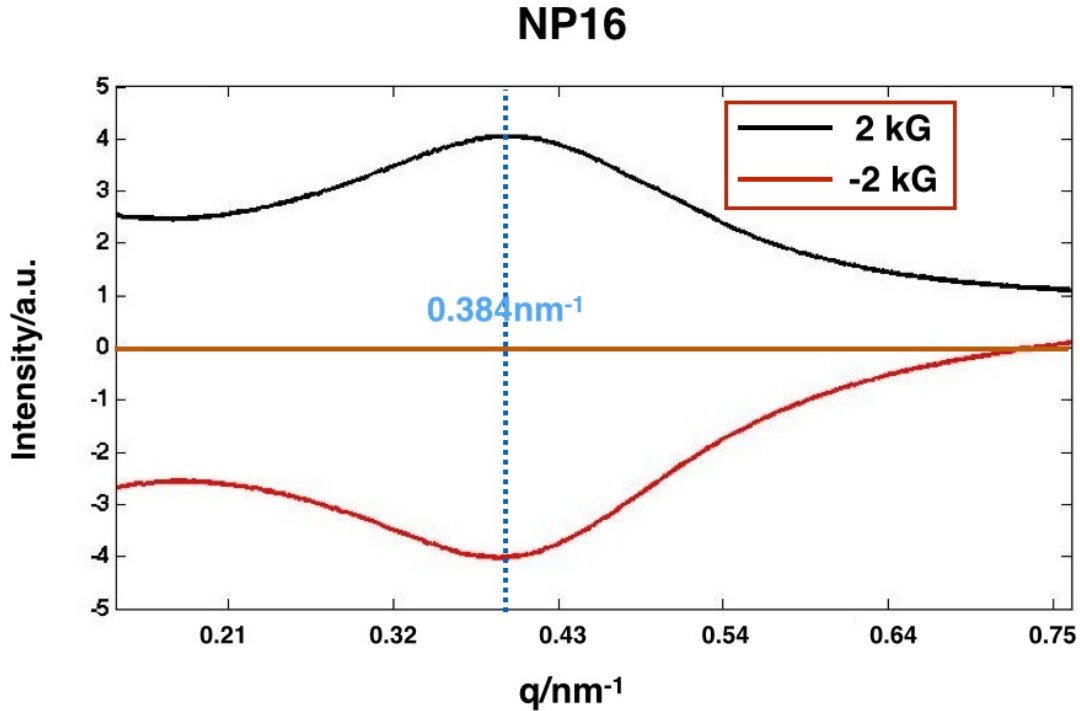
NP16

Figure 4.11 (a) The dichroic terms $\Delta I(q)$ plot as a function of q of NP16 (11.3 nm) at 80 K with a positive helicity. The peak position is at 0.384 nm^{-1}. When we switch the magnetic field, the sign of the dichroic profile will reverse.

The equation shows that $\Delta I(q)$ is proportional to $s_{c\text{-}m}(q)$. Therefore the charge-magnetic correlation $s_{c\text{-}m}(q)$ is also a function of q. It is expected that the magnetic moment of the nanoparticles will change direction when we switch the magnetic field from positive to negative and the term $s_{c\text{-}m}(q)$ will change sign accordingly. Now we look at the dichroic terms of sample NP16 at different field values in Figure 4.11. As expected, two dichroic terms at opposite field values have opposite signs. Also, the dichroic terms both show a peak at the same position as the intensity profile. The peak indicates the presence of a ferromagnetic order between nanoparticles. However, we want to point out that this dichroic profile is different from the original scattering profile. There may be a antiferromagnetic contribution in the dichroic profile too.

We will also look at the dichroic terms at different resonant energies. As we recall the W shape
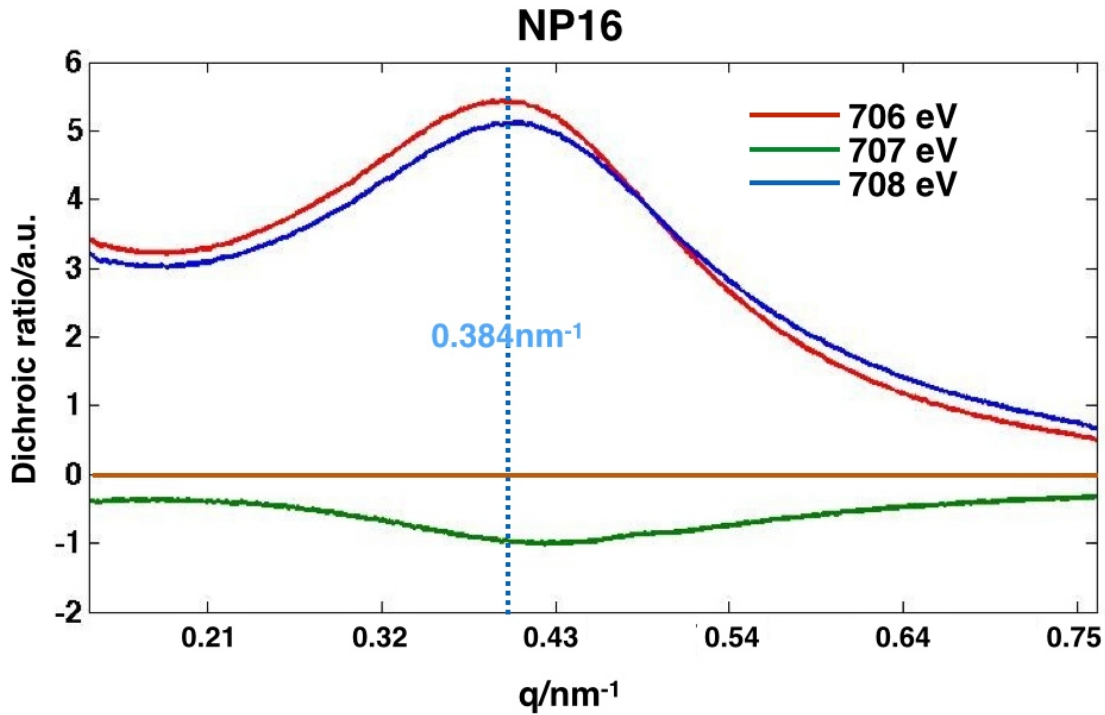
Figure 4.12 The dichroic terms $\Delta I(q)$ of sample NP16 (11.3 nm) at resonant edges 706 eV, 707 eV and 708 eV. The peak position is at 0.384 nm^{-1}.

of the XMCD signal, peak B corresponds to spin-down Fe^{3+} ions while peak A and C correspond to spin-up Fe^{2+} and Fe^{3+} ions. In Figure 4.12, we show the dichroic terms at peak $E_A = 706eV$, $E_B = 707eV$, and $E_C = 708eV$ of NP16 at 80 K. The field is 6.3 kG. It has been found that the dichroic term at 707 eV has the opposite sign compared to the dichroic terms at 706 eV and 708 eV. This is because the spin-up and spin-down Fe ions have a different coupling with photon spin, resulting in different signs of $s_{c-m}(q)$. The peak height of different dichroic term also varies with energy. Back in Figure 3.8 of the XMCD chapter, we found the W shape of NP16, with a 706 eV peak as the maximum and 707 eV as the minimum. This difference in XMCD signal originates from the different strengths of the photon spin and electron spin couplings. We found that the peak heights of the dichroic terms at different energies are also consistent with the XMCD results.

We also calculated the dichroic terms when the magnetic field applied on the sample is 0 kG,
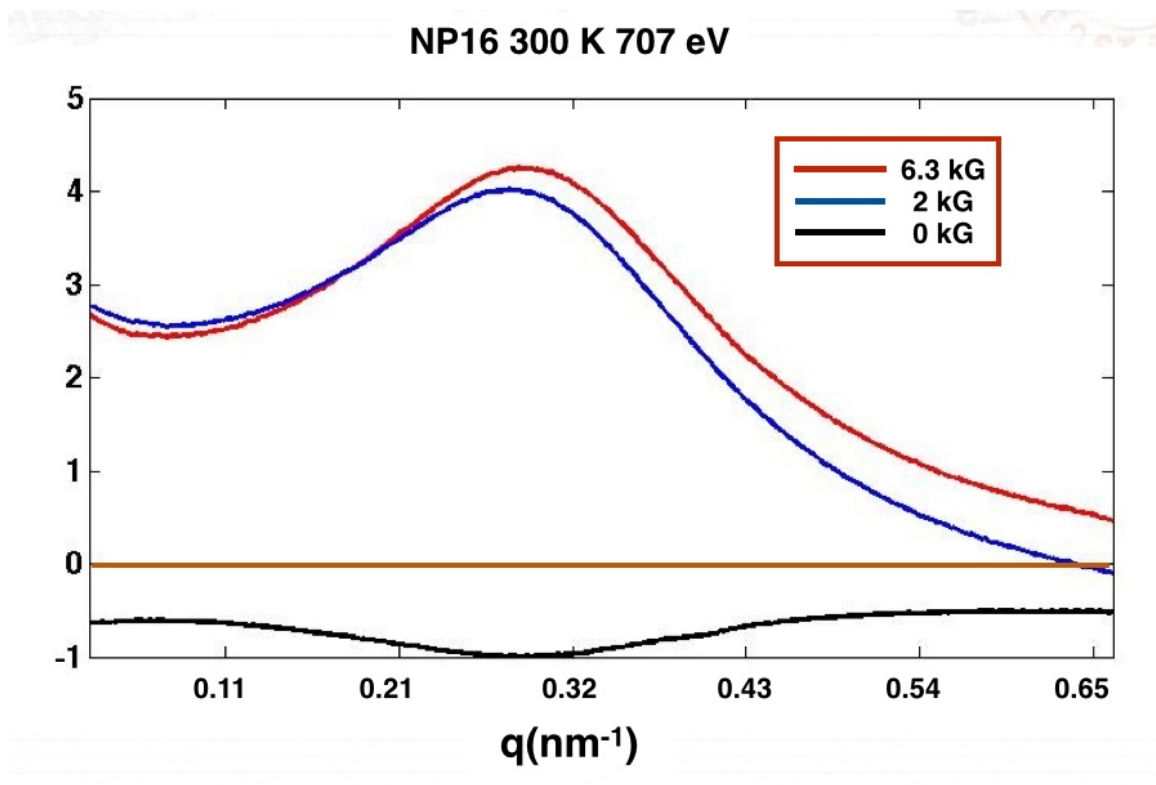
Figure 4.13 The dichroic terms $\Delta I(q)$ of sample NP16 (11.3 nm) at 0 kG, 2 kG and 6.3 kG. The temperature is 300 K. The intensity of the dichroic term at 0 kG is significantly lower than the other two.

2 kG and 6.3 kG as shown in Figure 4.13. The dichroic term at 6.3 kG has a higher peak than the dichroic term at 2 kG. This is because the photon spin and electron spin coupling is stronger when there is a higher field applied to the sample. Thus the magnetic signal is stronger. We can also see that the dichroic term at 0 kG has a very low intensity. It has a negative sign because there is a remnant magnetic moment in the sample when we tuned the magnetic field to 0 kG.

The dichroic term of NP18 shown in Figure 4.14 also shares the same peak as the scattering intensity profile of NP18. This means that magnetic moments of almost all of the nanoparticles are aligned with the magnetic field. The curve doesn't go to zero very steeply at the lower q range. This indicates that there might be a little antiferromagnetic contribution in the sample.
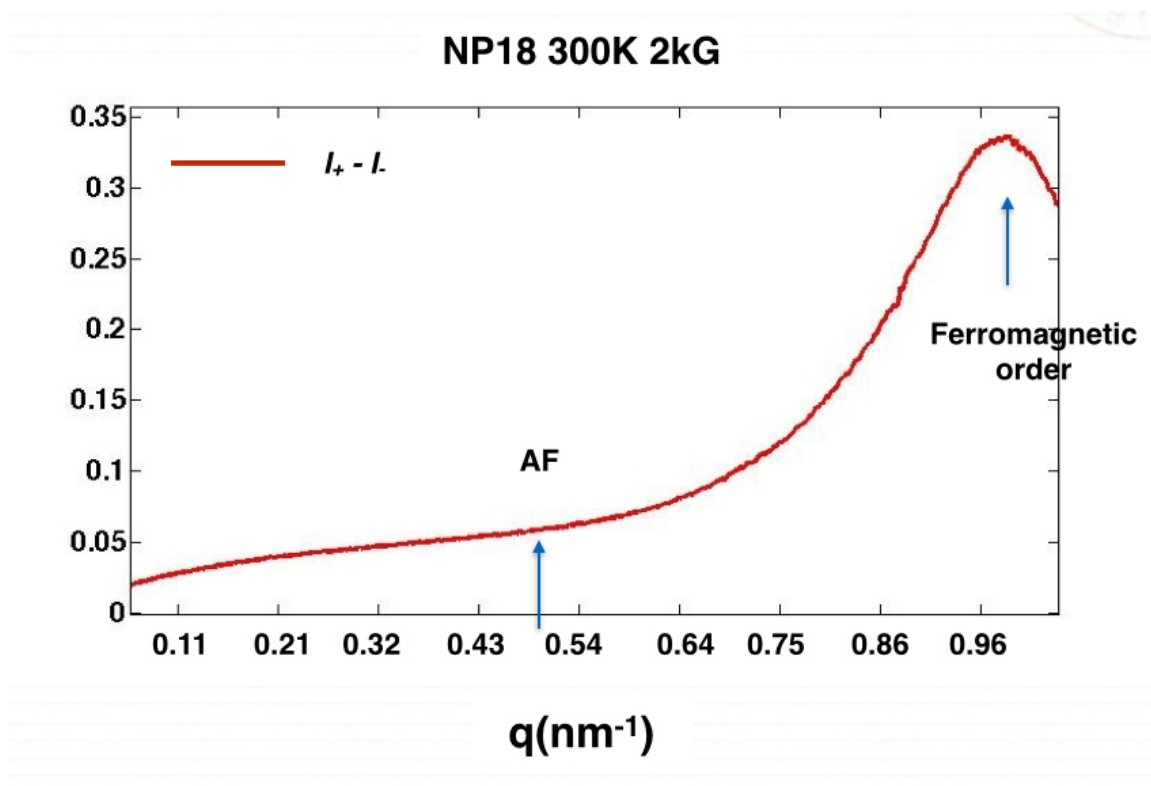
Figure 4.14 The dichroic term $\Delta I(q)$ of sample NP18 (5.6 nm) at 2 kG. The temperature is 300 K. The blue arrows indicate the ferromagnetic and anti-ferromagnetic order peaks in the curve.

4.6 Linear intensity profiles at different fields

Besides the dichroic term $I_+ - I_-$, we look at I_{linear} to extract the magnetic-magnetic correlation s_{m-m}. I_{linear} is defined as:

$$I_{linear} = \frac{I_+ + I_-}{2} \tag{4.10}$$

We take the difference of the I_{linear} at 2 kG and at 0 kG. Using the Equation 4.4 and 4.10, we got:

$$\Delta I_{\text{linear}}(q) = I_{\text{lin},H_1}(q) - I_{\text{lin},H_2}(q) = f_m^2 \Delta s_{m\text{-}m}(q) \tag{4.11}$$

As shown in Equation 4.11 that $\Delta I_{\text{linear}(q)}$ is proportional to $\Delta s_{m\text{-}m}$. In order to study the magnetic-magnetic correlation $s_{m\text{-}m}(q)$, we evaluated $\Delta I(q)$ as a function of q. In Figure 4.15, we display $I_{\text{lin},2\text{kG}}(q) - I_{\text{lin},0\text{kG}}(q)$ and $I_{\text{lin},-2\text{kG}}(q) - I_{\text{lin},0\text{kG}}(q)$. Because $f_{m\text{-}m}^2$ is a constant term and $s_{m\text{-}m}(q)$ is independent of the orientation of magnetization, the $I_{\text{lin},2\text{kG}}(q) - I_{\text{lin},0\text{kG}}(q)$ should preserve the same sign as $I_{\text{lin},-2\text{kG}}(q) - I_{\text{lin},0\text{kG}}(q)$. This is confirmed in Figure 4.15. We believe the differences between the two curves are mostly from the mechanical instabilities in the experimental setup. Some minor reasons can be the normalization process and the magnetic field calibration. Both curves share the same peak position as the charge scattering has, this also confirms the existence of ferromagnetic order in the nanparticles.
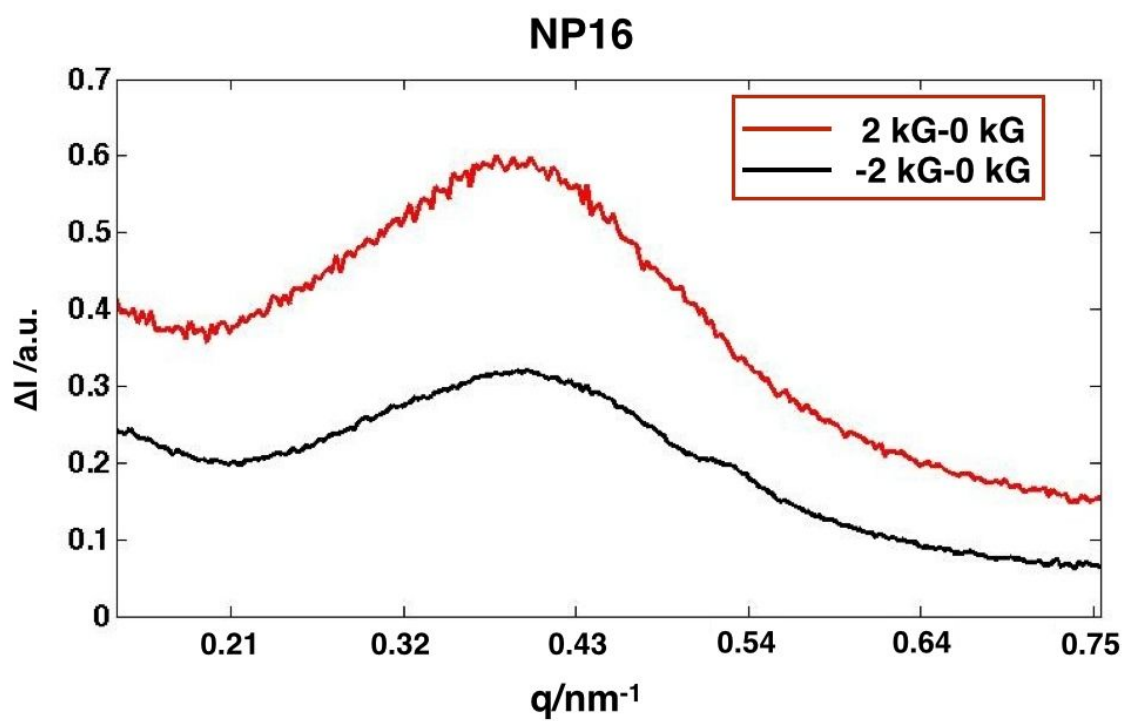
Figure 4.15 Calculated $I_{\mathrm{lin,2kG}}(q) - I_{\mathrm{lin,0kG}}(q)$ and $I_{\mathrm{lin,-2kG}}(q) - I_{\mathrm{lin,0kG}}(q)$ plot as a function of q of sample NP16 with positive helicity at 300 K.

Chapter 5

Conclusion

Using thermal decomposition of an iron precursor and the coating of particles with oleic acid, we have prepared Fe_3O_4 magnetic nanoparticles varying in size from 5 nm to 11 nm. A cubic $Fd3m$ structure, consistent with the inverse spinel structure of Fe_3O_4 magnetite, has been confirmed by XRD measurements. We have also applied the Scherrer equation to XRD data to estimate the particle size. A statistical analysis has also been used on the TEM images we took, which confirms the size of the particles as well. The results from XRD and TEM are in agreement with each other over a reasonable range. The discrepancy is within 1 nm.

By adjusting the solution concentration, we have also made a self-assembled single layer of nanoparticles on a Si_3N_4 membrane. We brought these membranes to SSRL to perform our XMCD and XRMS synchrotron experiments. With the XMCD data, we have been able to identify the $L_{3,2}$ resonant edges of Fe. We have also separated the spin and orbital magnetic moments by using sum rules. The quenching orbital moment and large spin moment we got are in agreement with the results reported from other groups. We have also found the magnetic moment in our nanoparticles is smaller than in bulk Fe_3O_4 . Furthermore, we have also found that the spin moment at low temperature is higher than at high temperature. We have concluded that the reduced magnetic moments can be attributed to the preparation methods, the electronic properties at the surface and

disorder effects.

We have also performed magnetic resonant scattering by tuning the x-ray energy to the resonant edges of Fe_3O_4. We have generated the scattering intensity profiles by using a spatial normalization and a time normalization. From the profiles, we estimated the interparticle distance between nanoparticles and the correlation length. This interparticle distance is consistent with the TEM analysis. With the study of profiles, we have also found NP18 is more closely-packed than NP16. We have also found that the scattering intensity on the edge is much stronger than off the edge. Calculation of the dichroic terms has also been performed to obtain the magnetic signal. The dichroic terms we obtained have confirmed that we got a true magnetic signal. We have also used the linear polarized profile I_{linear} to evaluate $I_{\text{lin,H}_1}(q) - I_{\text{lin,H}_2}(q)$. With this study, we concluded that there is an ferromagnetic magnetic order in the sample and there may also be some antiferromagnetic contribution in the sample.

Bibliography

[1] N. A. Frey, S. Peng, K. Cheng, and S. Sun, "Magnetic nanoparticles: synthesis, functionalization, and applications in bioimaging and magnetic energy storage," Chem. Soc. Rev. **38,** 2532 (2009).

[2] S. Mornet, S. Vasseur, F. Grasset, and E. Duguet, "Magnetic nano particle design for medical diagnosis and therapy," J. Mater. Chem. **14,** 2161 (2004).

[3] E. Duguet, S. Vasseur, S. Mornet, and J. M. Devoisselle, "Magnetic nanoparticles and their applications in medicine," Nanomedicine **1(2),** 157 (2006).

[4] J. H. Gao, H. W. Gu, and B. Xu, "Multifunctional Magnetic Nanoparticles: Design, Synthesis, and Biomedical Applications," Acc. Chem. Res. **42(8),** 1097 (2009).

[5] A. Ito, M. Shinkai, H. Honda, and T. Kobayashi, "Medical application of functionalized magnetic nanoparticles," J. Biosci. Bioeng. **100(1),** 1 (2005).

[6] E. J. Verwey, "Electronic Conduction of Magnetite (Fe_3O_4) and its Transition Point at Low Temperatures," Nature **144,** 327 (1939).

[7] C. P. Bean and J. D. Livingston, "Superparamagnetism," J. Appl. Phys. **30(4),** S120 (1959).

[8] S. Sun and H. Zeng, "Size-Controlled Synthesis of Magnetite Nanoparticles," J. Am. Chem. Soc. **124,** 8204 (2002).

[9] S. Sun, H. Zeng, D. B. Robinson, S. Raoux, P. M. Rice, S. X. Wang, and G. Li, "Monodisperse MFe_2O_4 (M=Fe, Co, Mn) Nanoparticles," J. Am. Chem. Soc. **126,** 273 (2004).

[10] X. Batlle and A. Labarta, "Finite-size effects in fine particles: magnetic and transport properties," J. Phys. D **35,** R15 (2002).

[11] P. Guardia, N. Prez, A.Labarta, and X. Batlle, "Controlled Synthesis of Iron Oxide Nanoparticles over a Wide Size Range," Langmuir **26(8),** 5843 (2010).

[12] J. Salafranca, J. Gazquez, N. Prez, A. Labarta, S. T. Pantelides, S. J. Pennycook, X. Batlle, and M. Varela, "Surfactant Organic Molecules Restore Magnetism in Metal-Oxide Nanoparticle Surfaces," Nano Lett. **12,** 2499 (2012).

[13] P. Guardia, J. Prez-Juste, A. Laharte, X. Batlle, and L. M. Liz-Marzn, "Heating rate influence on the synthesis of iron oxide nanoparticles:the case of decanoic acid," Chem. Commun **46,** 6108 (2010).

[14] J. Park, K. An, H. Y, J. Park, H. Noh, J. Kim, J. Park, N. Huang, and T. Hyeon, "Ultra-large-scale syntheses of monodisperse nanocrystals," Nature Materials **3,** 891 (2004).

[15] N. R. Jana, Y. F. Chen, and X. G. Peng, "Size- and Shape-Controlled Magnetic (Cr, Mn, Fe, Co, Ni) Oxide Nanocrystals via a Simple and General Approach," Chem. Mater. **16,** 3931 (2004).

[16] C. Altavilla, E. Ciliberto, D. Gatteschi, and C. Sangregorio, "A New Route to Fabricate Monolayers of Magnetite nano particles on Silicon," Advanced Materials **17(8),** 1084 (2005).

[17] G. F. Gaya, T. S. Berqu, and F. C. Fonseca, "Static and dynamic magnetic properties of spherical magnetite nanoparticles," J. Appl. Phys. **94,** 5 (2003).

[18] P. Tartaj, T. Gonzlez-Carreño, and C. J. Serna, "Single-Step Nanoengineering of Silica Coated Maghemite Hollow Spheres with Tunable Magnetic Properties," Adv. Mater. **13,** 1620 (2001).

[19] P.Guardia, B. Batlle-Brugal, A. G. Roca, O. Iglesias, M. P. Morales, C. J. Serna, A. Labarta, and X. Batlle, "Surfactant effects in magnetite nanoparticles of controlled size," J. Magn. Magn. Mater. **316,** e756 (2007).

[20] P. Tartaj, M. D. P. Morales, S. Veintemillas-Verdaguer, T. Gonzlez-Carreño, and C. J. Serna, "The preparation of magnetic nanoparticles for applications biomedicine," J. Phys. D **36,** R182 (2003).

[21] M. Blanco-Mantecn and K. O'Grady, "Interaction and size effects in magnetic nanoparticles," J. Magn. Magn. Mater. **296,** 124 (2006).

[22] X. Batlle, N. Prez, P. Guardia, O. Iglesias, A. Labarta, F. Bartolom, L. M. Garca, J. Bartolom, and A. G. Roca, "Magnetic nanoparticles with bulklike properties," J. Appl. Phys. **109,** 07B524 (2011).

[23] A. I. Figueroa, C. Moya, J. Bartolom, L. M. Garca, N. Prez, A. Labarta, and X. Batlle, "SiO_2 coating effects in the magnetic anisotropy of $Fe_{3-x}O_4$ nanoparticles suitable for bio-applications," J. Appl. Phys. **109,** 07B524 (2011).

[24] J. L. Erskine and E. A. Stern, "Calculation of the M_{23} magneto-optical absorption spectrum of ferromagnetic nickel," Phys. Rev. B **12,** 5016 (1975).

[25] G. Schütz, W. Wagner, W. Wilhelm, P. Kienle, R. Zeller, R. Frahm, and G. Materlik, "Absorption of circularly polarized x-rays in iron," Phys. Rev. Lett. **58,** 737 (1987).

[26] C. T. Chen, Y. U. Idzerda, H. J. Lin, N. V. Smith, G. Meigs, E.Chaban, G. H. Ho, E. Pellegrin, and F. Sette, "Experimental Confirmation of the X-Ray Magnetic Circular Dichroism Sum Rules for Iron and Cobalt," Phys. Rev. Letts. **75,** 152 (1995).

[27] A. Yamasaki, H. Kobori, H. Osawa, T. Nakamura, and A. Sugimura, "Soft x-ray magnetic circular dichroism study of magnetite nanoparticles," J. of Physics. **150,** 042235 (2009).

[28] B. T. Thole, P. Carra, F. Sette, and G. van der Lann, "X-Ray Circular Dichroism as a Probe of Orbital Magnetization," Phys. Rev. Letts. **68,** 12 (1992).

[29] D. J. Huang, C. F. Chang, H. T. Jeng, G. Y. Guo, H. J. Lin, W. B. Wu, H. C. Ku, A. Fujimori, Y. Takahashi, and C. T. Chen, "Spin and Orbital Magnetic Moments of Fe_3O_4," Phys. Rev. Lett. **93,** 7 (2004).

[30] E. Goering, M. Lafkioti, S. Gold, and G. Schütz, "Absorption spectroscopy and XMCD at the Verwey transition of Fe_3O_4," J. Magn. Magn. Mat. **310,** e249 (2007).

[31] E. Goering, S. Gold, M. Lafkioti, and G. Schütz, "Vanishing Fe 3d orbital moments in single-crystalline magnetite," Europhys. Letts. **73(1),** 97 (2006).

[32] E. Goering, M. Lafkioti, and S. Gold, "Comment on Spin and Orbital Magnetic Moments of Fe_3O_4," Phys. Rev. Lett. **96,** 039701 (2006).

[33] N. Púrez, F. Bartolomé, L. M. García, J. Bartolomé, M. P. Morales, C. J. Serna, A. Labarta, and X. Batlle, "Nanostructural origin of the spin and orbital contribution to the magnetic moment in $Fe_{3-x}O_4$ magnetite nanoparticles," Appl. Phys. Lett. **75,** 152 (2004).

[34] D. Ortega, E. Vélez-Fort, D. A. García, R. García, R. Litrín, C. Barrera-Solano, M. R. del Solar, and M. Domínguez, "Size and surface effects in the magnetic properties of maghemite and magnetite coated nanoparticles," Phil. Trans. R. Soc. A **368,** 4407 (2010).

[35] P. Platzman and N. Tzoar, "Magnetic Scattering of X Rays from Electrons in Molecules and Solids," Phys. Rev. B **2,** 3556 (1970).

[36] F. de Bergevin and M. Brunel, "Diffraction of X-rays by Magnetic Materials. I. General Formulae and Measurements on Ferro- and Ferrimagnetic Compounds," Acta Cryst. A **37,** 314 (1981).

[37] D. Gibbs, D. R. Harshman, E. D. Isaacs, D. B. McWhan, D. Mills, and C. Vettier, "Polarizationand Resonance Properties of Magnetic X-Ray Scattering in Holmium," Phys. Rev. Lett. **61,** 1241 (1988).

[38] J. P. Hannon, G. T. Trammell, M. Blume, and D. Gibbs, "X-Ray Resonance Exchange Scattering," Phys. Rev. Lett. **61,** 1245 (1988).

[39] G. van der Laan and B. T. Thole, "Strong magnetic x-ray dichroism in 2p absorption spectra of 3d transition-metal ions," Phys. Rev. B **43,** 13401 (1991).

[40] B. T. Thole, G. van der Laan, J. C. Fuggle, G. A. Sawatzky, R. C. Karnatak, and J. M. Esteva, "3d x-ray-absorption lines and the $3d^9 4f^{n+1}$ multiplets of the lanthanites," Phys. Rev. B **32,** 5107 (1985).

[41] J. B. Kortright, O. Hellwig, K. Chesnel, S. Sun, and E. E. Fullerton, "Interparticle magnetic correlations in dense Co nanoparticle assemblies," Phys. Rev. B **71,** 012402 (2005).

[42] J. B. Kortright, S.-K. Kim, G. P. Denbeaux, G. Zeltzer, K. Takano, and E. E. Fullerton, "Soft-x-ray small-angle scattering as a sensitive probe of magnetic and charge heterogeneity," Phys. Rev. B **64,** 092401 (2001).